COLLEGE OF ENGINEERING
NUCLEAR ENGINEERING & RADIOLOGICAL SCIENCES
UNIVERSITY OF MICHIGAN

Nuclear Reactor
Analysis & Methods
Group
NuRAM

NE/8887/2020-003-00
NURAM-2020-005-00

Global and Local Reactivity Assessments for Passive Control Systems of Multi-module HTGR Special Purpose Reactors

Brendan Kochunas, Kaitlyn Barr, Shai Kinast, and Sooyoung Choi

University of Michigan

09/30/2020

NEUP Nuclear Energy University Program
U.S. Department of Energy

This page is intentionally blank.

REVISION LOG

Revision	Date	Affected Pages	Revision Description
0	09/30/2020	All	Initial Release

Document pages that are:

Export Controlled:	None
IP/Proprietary/NDA Controlled:	Not Yet Assessed
Sensitive Controlled:	None
Unlimited:	Not Yet Assessed

This work was supported by funding received from the DOE Office of Nuclear Energy's Nuclear Energy University Program under contract number DE-NE0008887.

COLLEGE OF ENGINEERING
NUCLEAR ENGINEERING & RADIOLOGICAL SCIENCES
UNIVERSITY OF MICHIGAN

Argonne NATIONAL LABORATORY

HolosGen™

EXECUTIVE SUMMARY

In this report various categories of Flexible Power Operation (FPO) were defined. For each category the requisite reactivity for meeting the FPO specifications was quantified using a point kinetics reactor model with 3-temperature feedback. This data is given in Table EC.1.

Table EC.1. Summary of Reactivity Requirements for Load Follow by Category

Category	Ramp Rate ($\%P_r$/min)	Power Range Low / High ($\%P_r$)	Required $\lvert\rho\rvert$ (pcm)	Note
1	3 - 5	50 - 100	758	EUR [1]
2	20	50 - 100	759	EUR, emergency [1]
3	5	50 - 100	758	USA, EPRI, INPO [2]
4	1	75 - 100	379	Belgium [2]
5	10	20 - 100	1213	Germany, design limit [2]
6	10 5 2	80 - 100 50 - 100 20 - 100	1214	Germany, operational limit [2]
7	10	0 - 100	1517	PBMR [**?**]

The available reactivity in the reactor through temperature perturbations and the existing control drum systems were then quantified. A comparison of the reactivity from various control drum patterns is shown in Fig. EC.1, and the spatially dependent reactivity coefficients are shown in Figs. EC.2 and EC.3. When evaluating the available reactivity from each of these mechanisms it was found that:

- the existing control drum system would be sufficient for meeting reactivity requirements for any of the categorized FPO requirements.
- the reactivity available through varying the flow rate was not sufficient for any of the FPO categories.

Therefore, work in future milestones for this project will focus on the control drum system and automation for FPO. However, the concept of the passive flow controllers may still have value in other applications in the reactor performance such as: local power shaping, additional margin and protection in over-temperature transients, and small power changes (e.g. < 10% rated power). Likely some additional investigation will be performed to assess this value as well.

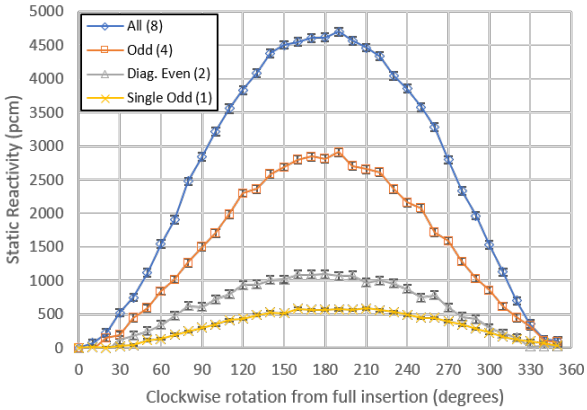

Figure EC.1. Comparisons of Integral Drum Worths for Different Patterns

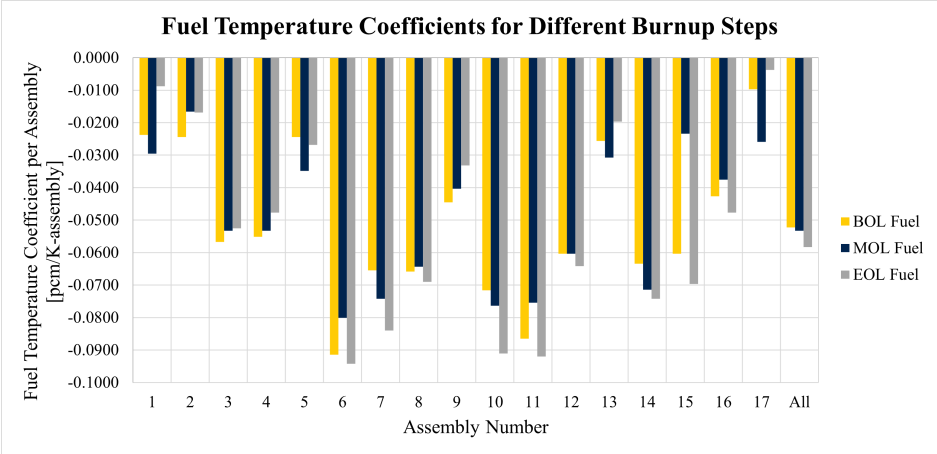

Figure EC.2. Fuel Temperature Coefficient (FTC) per assembly for each assembly at different burnups.

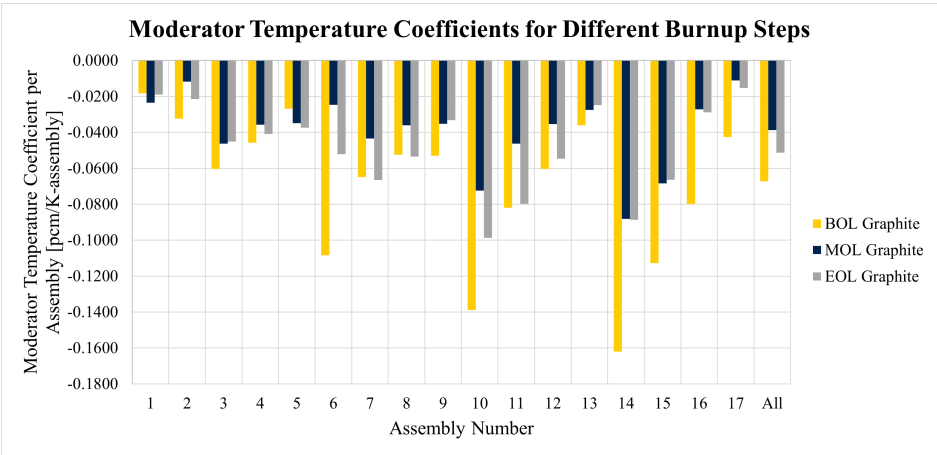

Figure EC.3. Moderator Temperature Coefficient (MTC) per assembly for each assembly at different burnups.

CONTENTS

LIST OF FIGURES

LIST OF TABLES

ACRONYMS

ANL Argonne National Laboratory

BOL Beginning of Life

EOL End of Life

FTC Fuel Temperature Coefficient

FPO Flexible Power Operation

HTGR High Temperature Gas Reactor

MOL Middle of Life

MTC Moderator Temperature Coefficient

PVFCV Passive Variable Flow Control Valve

SAM Systems Analysis Module

SPM Subcritical Power Module

TH Thermal Hydraulics/Fluids

EPRI Electric Power Research Institute

EUR European Utilities Requirements

INPO Institute of Nuclear Power Operations

NPP Nuclear Power Plant

MPC Model Predictive Control

PBMR Pebble Bed Modular Reactor

1. INTRODUCTION

The overall aim of this project is to investigate and develop passive systems for autonomous control of High Temperature Gas Reactor (HTGR) special purpose reactors–or microreactors. In previous work [3, 4], we investigated the reactivity of local temperature perturbations as one mode of physics for passive control, and variable reflector cross sections as the other. In this report we extend our investigation of these concepts addressing some of the items listed in the future work of our previous work. Additionally, we develop reactivity requirements for control to meet certain classes of load-follow demand.

The specific objective is evaluate the reactivity envelope (e.g. achievable range of reactivity perturbations) of each concept in meeting the reactivity requirements of the various power maneuvers. From this evaluation we will then make a recommendation as to which concept to pursue for more detailed calculations and analysis to meet future milestones in this project.

1.1 Background

As a specific use case for an HTGR, we use the reactor design under development at Holos. The Holos-Quad design is a scaled down HTGR with the core being composed of four SPMs. Each SPM is effectively an independent closed loop Brayton cycle power conversion unit with a nuclear heat source in a tube-shell heat exchanger configuration. This effectively eliminates the balance of plant. In earlier designs of this reactor the four SPMs were configurable so that they will create a critical reactor. An illustration of the SPM is shown in Fig. 1 A publicly available preliminary

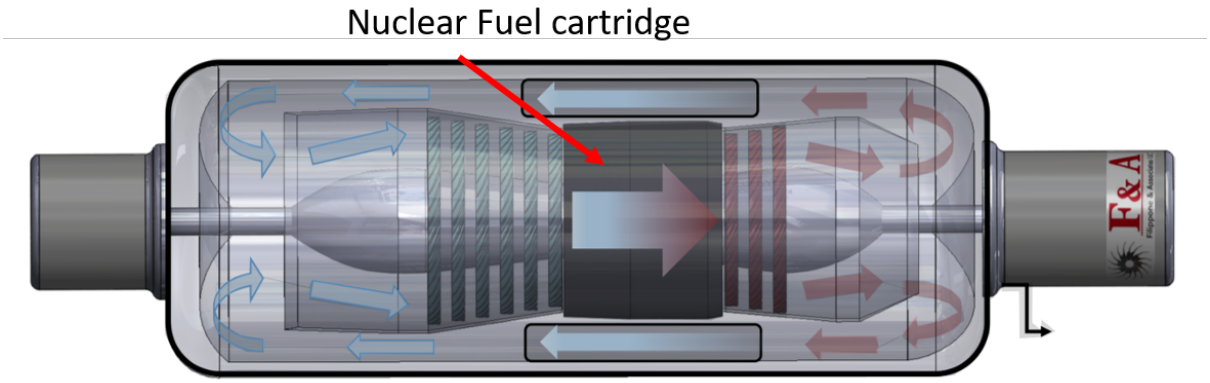

Figure 1. Illustration of an SPM

neutronic design of this reactor is described in [5]. The public design is illustrated in Fig. 2a with all SPMs inserted, and with SPMs separated in Fig. 2b.

However, since that time, the design has continued to evolve under the ARPA-E MEITNER program [6]. A new, proprietary design was developed by the ARPA-E Resource team at Argonne National Laboratory (ANL) and finalized on April 20th, 2020 [7]. The updated core design is the focus of the calculations and analysis of this report. In this reference design, the SPMs are still physically separated, but fixed in their quadrant, the SPMs are no longer actuated or moved to change reactivity. Additionally, there exists a central cruciform reflector between the SPMs. The final design still uses

8 control drums. The control drums from the preliminary design are shown in Section 1.1 with all drums in and out.

The reactivity control concepts discussed here look at the more conventional control drums and the concept of a Passive Variable Flow Control Valve (PVFCV). In the analysis of the control drums we present additional models for use in defining the reactivity worth curves of the drums–which would be essential for a control algorithm. In the analysis of the PVFCVs we examine the neutronic and thermal-fluid physics to define operational requirements for the valves.

1.2 Organization of this Report

The remainder of this report is organized as follow: first present our methodology and analysis for determining overall reactivity requirements for the control system. Next we present the results for quantifying the local temperature reactivity feedback control that would be utilized by the PVFCVs. Then we present a similar analysis to quantify the levels of reactivity control for different drum

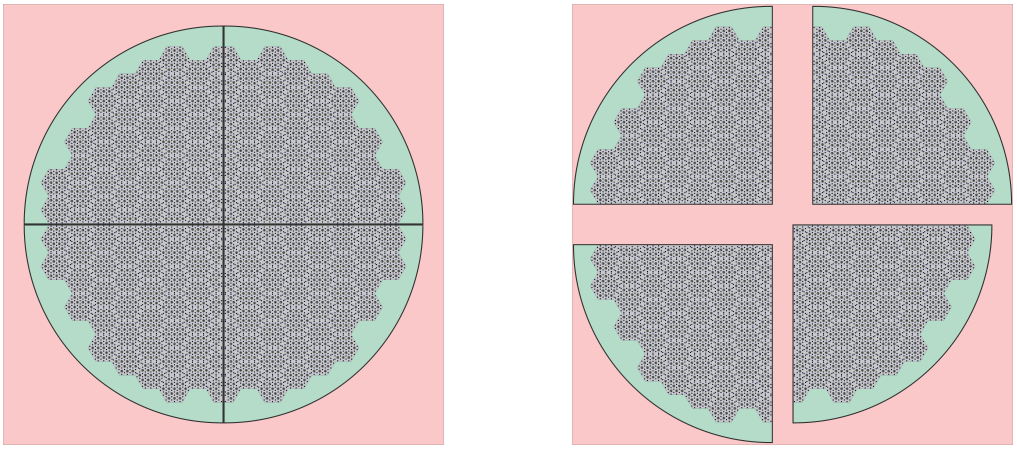

(a) Holos-Quad with SPMs together **(b) Holos-Quad with SPMs apart**

Figure 2. Preliminary Holos-Quad Design

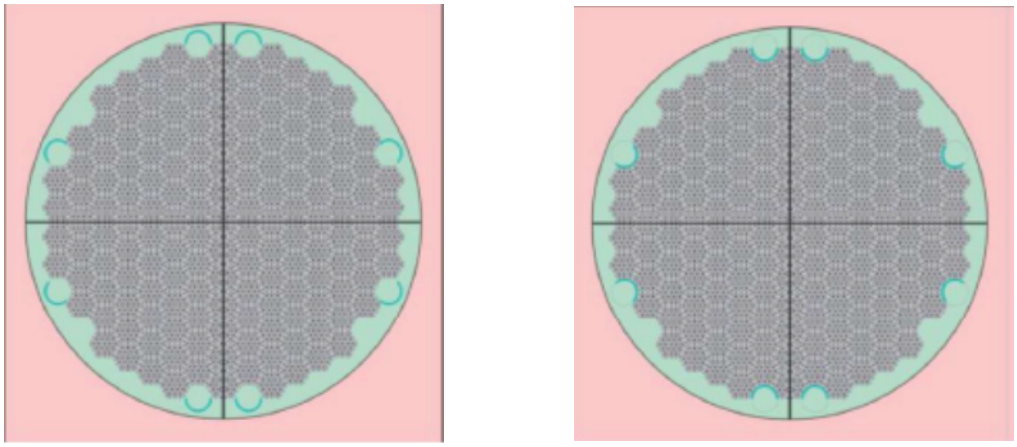

(a) Holos-Quad with Drums Out **(b) Holos-Quad with Drums In**

Figure 3. Preliminary Holos-Quad Control Drum Design

patterns. Finally we evaluate the two methods against the reactivity requirements developed in Section 2, and present a summary of the work, its conclusions, and near-term future activities.

2. REACTIVITY CONTROL SYSTEM REQUIREMENTS FOR FLEXIBLE POWER OPERATIONS

2.1 Description of Flexible Power Operational Requirements

The minimum requirements for the power maneuverability of modern reactors are defined by the grid operators. For example, according to the current version of the European Utilities Requirements (EUR), the Nuclear Power Plant (NPP) must at least be capable of daily load cycling operation between 50% and 100% of its rated power P_r, with a rate of change of 3-5%P_r/min. If the unit is requested to participate in emergency load variations, it shall at least be capable of load decreasing with 20%P_r/min [1].

NPPs in the USA are operated as baseload units, with only a few exceptions. Recently, investigative work has been initiated to support transitioning the US plants to FPO, as needed to support their regional grid needs and requirements. In the research performed by the Electric Power Research Institute (EPRI) and the Institute of Nuclear Power Operations (INPO), a load following between 50%P_r and 100%P_r with a maximum 5%P_r/min ramp rate is included [2].

In Belgium, a limited load following scheme is currently practiced on request from the grid system operator. The load following scheme includes operation between 75%P_r and 100%P_r with a maximum 1%P_r/min ramp rate [2].

In Germany, commissioning tests demonstrated that the load following scheme considered in the Konvoi reactor design was proven to allow for load change performance up to the design criteria. The design criteria allows load following with 10%P_r/min in a power range of 20-100%P_r. The plant commissioning test also confirmed the load factors of category 6 in Table 1 from the licensed operational manual [2].

In South Africa, the Pebble Bed Modular Reactor (PBMR) design team completed the conceptual design of the PBMR. For the PBMR design, power is allowed to change with 10%P_r/min ramp rate in a power range of 0-100%P_r [**?**].

To assess the requirements of the control system for load following, we first quantify the reactivity needed to meet each category of load follow defined in Table 1. The reactivity requirements are quantified using a simple point-reactor model with a 3-temperature thermal-fluid model and linear reactivity feedback. These models are described in detail in the next subsection.

Table 1. Summary of ramp rate requirements

Category	Ramp Rate ($\%P_r$/min)	Power Range Low / High ($\%P_r$)	Note
1	3 - 5	50 - 100	EUR [1]
2	20	50 - 100	EUR, emergency [1]
3	5	50 - 100	USA, EPRI, INPO [2]
4	1	75 - 100	Belgium [2]
5	10	20 - 100	Germany, design limit [2]
6	10 5 2	80 - 100 50 - 100 20 - 100	Germany, operational limit [2]
7	10	0 - 100	PBMR [?]

2.2 Quantification of Reactivity Requirements

2.2.1 Reactor Kinetics Model

At this point to model the reactor kinetics we use with point kinetics equations with 6 delayed groups. These equations are given as:

$$\frac{dn(t)}{dt} = \frac{\rho(t) - \beta}{\Lambda} n(t) + \sum_{i=1}^{m} \lambda_i C_i(t), \tag{1}$$

$$\frac{dC_i(t)}{dt} = \frac{\beta_i}{\Lambda} n(t) - \lambda_i C_i(t) \ , \quad i = 1, 2, ..., m, \tag{2}$$

where n is the neutron density; m is the number of delayed groups which is 6; ρ is the reactivity; β is the total effective delayed neutron fraction; β_i is the i-th group effective delayed neutron fraction; λ_i is the i-th group effective delayed neutron decay constant; Λ is the generation time; and C_i is the i-th group precursor concentration.

The initial condition of the precursor concentration at steady-state is derived by setting the left side of Eq. (2) to be zero as follows:

$$C_{i0} = \frac{\beta_i n_0}{\lambda_i \Lambda} \ , \quad i = 1, 2, ..., m, \tag{3}$$

where the subscript 0 denotes the initial steady-state condition.

Using Eq. (3), the normalized point kinetics equations are written as follow:

$$\frac{d\bar{n}(t)}{dt} = \frac{\rho(t) - \beta}{\Lambda} \bar{n}(t) + \sum_{i=1}^{m} \frac{\beta_i}{\Lambda} \bar{C}_i(t), \tag{4}$$

$$\frac{d\bar{C}_i(t)}{dt} = \lambda_i \bar{n}(t) - \lambda_i \bar{C}_i(t) \ , \quad i = 1, 2, ..., m, \tag{5}$$

where $\bar{n}(t)$is $n(t)/n_0$, and $\bar{C}_i(t)$ is $C_i(t)/C_{i0}$.

The reactivity feedback model has the components for reactivity due to the control systems and passive feedback mechanisms. The Holos reactor has two ways to actively control reactivity. One is moving one of SPMs. The other is rotating drums simultaneously. In this study, the control drum is only considered as the active reactivity control model because the SPM movement has been eliminated from the design. The reactivity model with the control drum and various temperature feedback mechanisms is defined as follows:

$$\delta\rho(t) = \delta\rho_d(t) + \alpha_f \delta T_f(t) + \alpha_m \delta T_m(t) + \alpha_c \delta T_c(t), \tag{6}$$

$$\frac{d\delta\rho_d(t)}{dt} = G_d Z_d(t), \tag{7}$$

where $\delta\rho_d$ is the reactivity change due to control system (drums); α_f is the reactivity coefficient of fuel; α_m is the reactivity coefficient of moderator; α_c is the reactivity coefficient of coolant; $\delta T_f(t)$, $\delta T_m(t)$, and $\delta T_c(t)$ are the temperature changes of the fuel, moderator, and coolant, respectively. Generally speaking, G_d is the differential reactivity worth of control drums, and Z_d is the velocity of the control drum. However, in our case we are assuming it is some externally imposed reactivity from a control system.

The kinetics parameters and the reactivity coefficients used in the model are listed in Table 2. These come from various references which are documented in [8] and also from the calculations described in Sections 3 and 4

2.2.2 3-Temperature Thermal-fluids Model

For the thermal-fluids dynamic response, we consider the 3-temperature model of a point reactor– which should be reasonable for slow transients as studied here. Validation against SAM is a future activity. We treat the heat-balance equations of the fuel, moderator and coolant temperatures as:

$$m_f c_f \frac{dT_f(t)}{dt} = qP_r\bar{n}(t) - K_{fm}\left(T_f(t) - T_c(t)\right), \tag{8}$$

$$m_m c_m \frac{dT_m(t)}{dt} = (1-q)\,P_r\bar{n}(t) + K_{fm}\left(T_f(t) - T_m(t)\right) - K_{mc}\left(T_m(t) - T_c(t)\right), \tag{9}$$

$$m_c c_c \frac{dT_c(t)}{dt} = K_{mc}\left(T_m(t) - T_c(t)\right) - 2\dot{m}_c c_c\left(T_c(t) - T_{c,in}\right), \tag{10}$$

where P_r is the rated power of reactor; the dimensionless parameter q represents the fraction of heat deposited in the fuel (the rest being deposited in the moderator); m_f, m_m, and m_c are the masses of fuel, moderator, and coolant, respectively; $\dot{m}_c$ is the coolant flow rate; c_f, c_m, and c_c are the heat capacities of fuel, moderator, and coolant, respectively; K_{fm} and K_{mc} are the heat transfer coefficients from fuel to moderator, and from moderator to coolant, respectively; and $T_{c,in}$ is the inlet coolant temperature. The heat transfer coefficients that were used were computed from the SAM results discussed in Section 3.

The thermal-fluids parameters are also listed in Table 2.

2.2.3 State-Space Reactor Model Description

We now wish to obtain the reactivity response for the load follow categories outlined in Table 1. To accomplish this, we formulate a time-dependent control problem. This begins with converting

Table 2. Coefficients of mathematical models

Parameter	Value	Unit
β	480.10	pcm
β_1	14.20	pcm
β_2	92.40	pcm
β_3	78.00	pcm
β_4	206.60	pcm
β_5	67.10	pcm
β_6	21.80	pcm
Λ	0.00168	s
λ_1	0.01270	1/s
λ_2	0.03170	1/s
λ_3	0.11600	1/s
λ_4	0.31100	1/s
λ_5	1.40000	1/s
λ_6	3.87000	1/s
α_f	-2.875	pcm/K
α_m	-3.696	pcm/K
α_c	0.000	pcm/K
G_d	-26.11	pcm/deg
P_r	22.00	MW
q	0.96	-
c_f	977.00	J/kg/K
c_m	1697.00	J/kg/K
c_c	5188.60	J/kg/K
m_f	2002.00	kg
m_m	11573.00	kg
m_c	500.00	kg
$\dot{m}_c$	17.50	kg/s
K_{fm}	1.17E+06	W/K
K_{mc}	2.16E+05	W/K

the mathematical models for the normalized point kinetics, reactivity, and thermal-fluids into a state-space model. The neutron density is written in the following deviation form:

$$\frac{d\delta\bar{n}(t)}{dt} = \frac{\bar{n}_0}{\Lambda}\delta\rho(t) - \frac{\beta}{\Lambda}\delta\bar{n}(t) + \sum_{i=1}^{m}\frac{\beta_i}{\Lambda}\delta\bar{C}_i(t), \tag{11}$$

where the symbol δ indicates the deviation of a variable from an equilibrium value, *i.e.*, $x(t) = x_0 + \delta x(t)$. Inserting Eq. (6)) into Eq. (11) leads to:

$$\frac{d\delta\bar{n}(t)}{dt} = -\frac{\beta}{\Lambda}\delta\bar{n}(t) + \sum_{i=1}^{m}\frac{\beta_i}{\Lambda}\delta\bar{C}_i(t) + \frac{\bar{n}_0}{\Lambda}\left(\alpha_f\delta T_f(t) + \alpha_m\delta T_m(t) + \alpha_c\delta T_c(t) + \delta\rho_d(t)\right). \tag{12}$$

In a similar way, equations for the precursor density, fuel temperature, moderator temperature, and

coolant temperature are written as follow:

$$\frac{d\delta\bar{C}_i(t)}{dt} = \lambda_i \delta\bar{n}(t) - \lambda_i \delta\bar{C}_i(t), \tag{13}$$

$$\frac{d\delta T_f(t)}{dt} = \frac{qP_r}{m_f c_f}\delta\bar{n}(t) - \frac{K_{fm}}{m_f c_f}\left(\delta T_f(t) - \delta T_m(t)\right), \tag{14}$$

$$\frac{d\delta T_m(t)}{dt} = \frac{1-q}{m_m c_m} P_r \delta\bar{n}(t) + \frac{K_{fm}}{m_m c_m}\left(\delta T_f(t) - \delta T_m(t)\right) - \frac{K_{mc}}{m_m c_m}\left(\delta T_m(t) - \delta T_c(t)\right), \tag{15}$$

$$\frac{d\delta T_c(t)}{dt} = \frac{K_{mc}}{m_c c_c}\left(\delta T_m(t) - \delta T_c(t)\right) - \frac{2\dot{m}_c c_c}{m_c c_c}\delta T_c(t). \tag{16}$$

Equations (12) to (16) are linearized and written in the following state-space model form:

$$\left\{\begin{array}{l} \mathbf{x_c} = \mathbf{A_c x_c} + \mathbf{B_c u} \\ \mathbf{y} = \mathbf{C_c x_c} \end{array}\right\}, \tag{17}$$

where the system matrix is

$$\mathbf{A_c} = \begin{bmatrix} -\frac{\beta}{\Lambda} & \frac{\beta_1}{\Lambda} & \cdots & \frac{\beta_m}{\Lambda} & \frac{\bar{n}_0\alpha_f}{\Lambda} & \frac{\bar{n}_0\alpha_m}{\Lambda} & \frac{\bar{n}_0\alpha_c}{\Lambda} & \frac{\bar{n}_0}{\Lambda} \\ \lambda_1 & -\lambda_1 & \cdots & 0 & 0 & 0 & 0 & 0 \\ \vdots & \vdots & \vdots & \vdots & \vdots & \vdots & \vdots & \vdots \\ \lambda_m & 0 & \cdots & -\lambda_m & 0 & 0 & 0 & 0 \\ \frac{qP_r}{m_f c_f} & 0 & \cdots & 0 & -\frac{K_{fm}}{m_f c_f} & \frac{K_{fm}}{m_f c_f} & 0 & 0 \\ \frac{(1-q)P_r}{m_m c_m} & 0 & \cdots & 0 & \frac{K_{fm}}{m_m c_m} & -\frac{K_{fm}+K_{mc}}{m_m c_m} & \frac{K_{mc}}{m_m c_m} & 0 \\ 0 & 0 & \cdots & 0 & 0 & \frac{K_{mc}}{m_c c_c} & -\frac{K_{mc}+2\dot{m}_c c_c}{m_c c_c} & 0 \\ 0 & 0 & \cdots & 0 & 0 & 0 & 0 & 0 \end{bmatrix}, \tag{18}$$

and the state vector is

$$\mathbf{x_c} = \begin{bmatrix} \delta\bar{n}(t) & \delta\bar{C}_1(t) & \cdots & \delta\bar{C}_m(t) & \delta T_f(t) & \delta T_m(t) & \delta T_c(t) & \delta\rho_d(t) \end{bmatrix}^T. \tag{19}$$

The input matrix is

$$\mathbf{B_c} = \begin{bmatrix} 0 & 0 & \cdots & 0 & 0 & 0 & 0 & G_d \end{bmatrix}^T. \tag{20}$$

The control vector is

$$\mathbf{u} = \left[Z_d(t)\right]. \tag{21}$$

The output vector is

$$\mathbf{y} = \left[\delta\bar{n}(t)\right], \tag{22}$$

and finally the output matrix is

$$\mathbf{C_c} = \begin{bmatrix} 1 & 0 & \cdots & 0 & 0 & 0 & 0 & 0 \end{bmatrix}. \tag{23}$$

2.2.4 Model predictive control based assessment

To solve the state-space control problem derived in the previous section we use the Model Predictive Control (MPC) algorithm. MPC is an advanced method to control a process [9]. It is based on an iterative finite-horizon optimization of the system (*e.g.*, trajectory optimization). To minimize an error between a desired set-point and predicted output, control input is computed for a relatively short time horizon in the future by evaluating a cost function. This calculation is then repeated at each subsequent instant or time-window.

The following is derivation for MPC, that is based on [10]. The state-space model in Eq. (17) is written as the following discretized linear system.

$$\mathbf{x_m}(k+1) = \mathbf{A_m}\mathbf{x_m}(k) + \mathbf{B_m}\mathbf{u}(k), \tag{24}$$

$$\mathbf{y}(k) = \mathbf{C_m}\mathbf{x_m}(k), \tag{25}$$

where $\mathbf{A_m}$, $\mathbf{B_m}$, and $\mathbf{C_m}$ are the discrete forms of matrix A_c, B_c, and C_c , respectively.

Applying a difference approximation to Eq. (25), yields

$$\mathbf{x_m}(k+1) - \mathbf{x_m}(k) = \mathbf{A_m}\left(\mathbf{x_m}(k) - \mathbf{x_m}(k-1)\right) + \mathbf{B_m}\left(\mathbf{u}(k) - \mathbf{u}(k-1)\right), \tag{26}$$

which makes use of the following simplifying notation

$$\Delta(\cdot)(k) = (\cdot)(k) - (\cdot)(k-1). \tag{27}$$

Using this notation again inEq. (24) results in

$$\Delta\mathbf{x_m}(k+1) = \mathbf{A_m}\Delta\mathbf{x_m}(k) + \mathbf{B_m}\Delta\mathbf{u}(k). \tag{28}$$

Note that the input to the state-space model is $\Delta\mathbf{u_m}(k)$. The next step is to connect $\Delta\mathbf{x_m}(k)$ to the output $\mathbf{y_m}(k)$. To do so, a new state variable vector is defined as

$$\mathbf{x}(k) = \begin{bmatrix} \Delta\mathbf{x_m}(k)^T & \mathbf{y}(k) \end{bmatrix}^T. \tag{29}$$

Note that

$$\begin{aligned} \mathbf{y}(k+1) - \mathbf{y}(k) &= \mathbf{C_m}\left(\Delta\mathbf{x_m}(k+1)\right) \\ &= \mathbf{C_m}\mathbf{A_m}\Delta\mathbf{x_m}(k) + \mathbf{C_m}\mathbf{B_m}\Delta\mathbf{u}(k) \end{aligned}. \tag{30}$$

Combining Eqs. (28) and (30) leads to the following state-space model:

$$\overbrace{\begin{bmatrix} \Delta\mathbf{x_m}(k+1) \\ \mathbf{y}(k+1) \end{bmatrix}}^{\mathbf{x}(k+1)} = \overbrace{\begin{bmatrix} \mathbf{A_m} & \mathbf{o}_\mathbf{m}^T \\ \mathbf{C_m}\mathbf{A_m} & 1 \end{bmatrix}}^{\mathbf{A}} \overbrace{\begin{bmatrix} \Delta\mathbf{x_m}(k) \\ \mathbf{y}(k) \end{bmatrix}}^{\mathbf{x}(k)} + \overbrace{\begin{bmatrix} \mathbf{B_m} \\ \mathbf{C_m}\mathbf{B_m} \end{bmatrix}}^{\mathbf{B}} \Delta\mathbf{u}(k), \tag{31}$$

$$\mathbf{y}(k) = \overbrace{\begin{bmatrix} \mathbf{o}_\mathbf{m}^T & 1 \end{bmatrix}}^{\mathbf{C}} \begin{bmatrix} \Delta\mathbf{x_m}(k) \\ \mathbf{y}(k) \end{bmatrix}, \tag{32}$$

where $\mathbf{o_m} = \overbrace{\begin{bmatrix} 0 & 0 & \dots & 0 \end{bmatrix}}^{n_1}$; n_1 is the dimension of $\mathbf{x_m}$; and $\mathbf{A}$, $\mathbf{B}$, and $\mathbf{C}$ are called the augmented model, which will be used in the design of predictive control.

Assuming that at the sampling instant k_i, where $k_i > 0$, the state variable vector $\mathbf{x}(k_i)$ is available through measurement, then the state $\mathbf{x}(k_i)$ provides the current plant information. The future control trajectory is denoted by

$$\Delta\mathbf{u}(k_i),\ \Delta\mathbf{u}(k_i+1),\ \dots,\ \Delta\mathbf{u}(k_i+N_c-1), \tag{33}$$

where N_c is called the *control horizon*–dictating the number of parameters used to capture the future *control trajectory*. With the information given in $\mathbf{x}(k_i)$, the future state variables are predicted for N_p number of samples, where N_p is called the prediction horizon. N_p is also the length of the optimization window. We denote the future state variables as

$$\mathbf{x}(k_i|k_i),\ \mathbf{x}(k_i+1|k_i),\ \dots,\ \mathbf{x}(k_i+N_p|k_i), \tag{34}$$

where $\mathbf{x}(k_i+m|k_i)$ is the predicted state variable at k_i+m with given current plant information $\mathbf{x}(k_i)$. The control horizon N_c is chosen to be less than (or equal to) the prediction horizon N_p.

It is possible to denote the state-space model for the prediction horizons as follows:

$$\mathbf{Y} = \mathbf{F}\mathbf{x}(k_i) + \Phi\Delta\mathbf{U}, \tag{35}$$

where

$$\mathbf{Y} = \begin{bmatrix} \mathbf{y}(k_i+1|k_i) & \cdots & \mathbf{y}(k_i+N_p|k_i) \end{bmatrix}^T, \tag{36}$$

$$\Delta\mathbf{U} = \begin{bmatrix} \Delta\mathbf{u}(k_i) & \cdots & \Delta\mathbf{u}(k_i+N_c-1) \end{bmatrix}^T, \tag{37}$$

$$\mathbf{F} = \begin{bmatrix} \mathbf{CA} \\ \vdots \\ \mathbf{CA}^{N_p} \end{bmatrix}, \tag{38}$$

$$\Phi = \begin{bmatrix} \mathbf{CB} & 0 & 0 & \cdots & 0 \\ \mathbf{CAB} & \mathbf{CB} & 0 & \cdots & 0 \\ \mathbf{CA}^2\mathbf{B} & \mathbf{CAB} & \mathbf{CB} & \cdots & 0 \\ \vdots & & & & \\ \mathbf{CA}^{N_p-1}\mathbf{B} & \mathbf{CA}^{N_p-2}\mathbf{B} & \mathbf{CA}^{N_p-3}\mathbf{B} & \cdots & \mathbf{CA}^{N_p-N_c}\mathbf{B} \end{bmatrix}. \tag{39}$$

For a given set-point signal (or reference trajectory), the objective of the predictive control system is to bring the predicted output as close as possible to the set-point signal. It is assumed that the set-point signal remains constant in the optimization window. This objective is then translated into an input to find the 'best' control parameter vector $\Delta\mathbf{U}$ such that an error function between the set-point and the predicted output is minimized. The cost function J, that reflects the control objective, is defined as follows:

$$J = (\mathbf{R_s} - \mathbf{Y})^T\ (\mathbf{R_s} - \mathbf{Y}) + \Delta\mathbf{U}^T\bar{\mathbf{R}}\Delta\mathbf{U}, \tag{40}$$

where the data vector $\mathbf{R}_\mathbf{s}^T$ contains the set-point information $r(k_i)$ as follows:

$$\mathbf{R}_\mathbf{s}^T = \bar{\mathbf{R}}_\mathbf{s} r(k_i) = \overbrace{\begin{bmatrix} 1 & 1 & \cdots & 1 \end{bmatrix}}^{N_p} r(k_i). \tag{41}$$

In Eq. (40)), where the first term is linked to the objective of minimizing the errors between the predicted output $\mathbf{Y}$ and the set-point signal $\mathbf{R}_\mathbf{s}$ while the second term reflects the consideration given to the size of $\Delta\mathbf{U}$ when the objective function J is made to be as small as possible. $\bar{\mathbf{R}}$ is a diagonal matrix in the form that $\bar{\mathbf{R}} = r_w \mathbf{I}_{N_c \times N_c}$ $(r_w \geq 0)$ where r_w is used as a tuning parameter for the desired closed-loop performance. To find the optimal control input that will minimize J, J is expressed as follows by using Eqs. (35) and (40):

$$J = (\mathbf{R}_\mathbf{s} - \mathbf{F}\mathbf{x}(k_i))^T (\mathbf{R}_\mathbf{s} - \mathbf{F}\mathbf{x}(k_i)) - 2\Delta\mathbf{U}^T\Phi^T (\mathbf{R}_\mathbf{s} - \mathbf{F}\mathbf{x}(k_i)) + \Delta\mathbf{U}^T \left(\Phi^T\Phi + \bar{\mathbf{R}}\right) \Delta\mathbf{U}. \tag{42}$$

According to the extreme value theory of functions, when the derivative of J with respect to $\Delta\mathbf{U}$ (*i.e.,* $\partial J/\partial\Delta\mathbf{U}$) is zero, the objective function J gets its extreme values. The first derivative of J is

$$\frac{\partial J}{\partial \Delta\mathbf{U}} = 2\Phi^T (\mathbf{R}_\mathbf{s} - \mathbf{F}\mathbf{x}(k_i)) + 2\left(\Phi^T\Phi + \bar{\mathbf{R}}\right)\Delta\mathbf{U}. \tag{43}$$

From relation of $\partial J/\partial\Delta\mathbf{U} = 0$, the optimal solution is found as follows:

$$\begin{aligned} \Delta\mathbf{U} &= \left(\Phi^T\Phi + \bar{\mathbf{R}}\right)^{-1}\Phi^T (\mathbf{R}_\mathbf{s} - \mathbf{F}\mathbf{x}(k_i)) \\ &= \left(\Phi^T\Phi + \bar{\mathbf{R}}\right)^{-1}\Phi^T \left(\bar{\mathbf{R}}_\mathbf{s} r(k_i) - \mathbf{F}\mathbf{x}(k_i)\right) \end{aligned}, \tag{44}$$

where the matrix $\left(\Phi^T\Phi + \bar{\mathbf{R}}\right)^{-1}$ is called Hessian matrix in the optimization literature, and $\left(\Phi^T\Phi + \bar{\mathbf{R}}\right)^{-1}$ is assumed to exist.

Although the optimal parameter vector $\Delta\mathbf{U}$ contains the controls $\Delta\mathbf{u}(k_i), \Delta\mathbf{u}(k_i+1), \ldots, \Delta\mathbf{u}(k_i + N_c - 1)$, with the receding horizon control principle, the first sample of this sequence, *i.e.,* $\Delta\mathbf{u}(k_i)$, is implemented only while ignoring the rest of the sequence. When the next sample period arrives, the more recent measurement is taken to form the state vector $\mathbf{x}(k_i + 1)$ for calculation of the new sequence of control signal. This procedure is repeated in real time to give the receding horizon control law.

There are several types of constraints frequently encountered in control applications. The first two types deal with constraints imposed on the control variables $\mathbf{u}(k)$ and $\mathbf{\Delta u}(k)$. The third type of constraint deals with output $\mathbf{y}(k)$ or state variable $\mathbf{x}(k)$ constraints. In our application, only the constraints imposed on the control variables are considered. The constraints on the amplitude of the control variable, *i.e.,* the rotation rate of control rod (or reactivity ramp rate), are specified in the form:

$$\mathbf{u}^{\min} \leq \mathbf{u} \leq \mathbf{u}^{\max}. \tag{45}$$

The state-space model with the MPC algorithm is implemented in a test code. Figures 4 and 5 show the simulation results. The reference power trajectory is chosen to have a power ramp rate of $\pm 10\% P_r$/min. The transition of power occurs at 5 min $\sim$ 15 min and 40 min $\sim$ 50 min.

As shown in Figure 4, the MPC controller follows the desired power accurately. There is no noticeable error between the reference power and calculated power. The temperatures changes from the initial state are also presented in the figure. The temperature change overall lags the power trajectory.

Figure 5 shows the rotation and rotation rate of the control drum. A rotation-independent differential worth of 26.11 pcm/deg is used in the simulation. This value is consistent with assuming that all control drums are rotated simultaneously. The mechanical constraint applied to the rotation rate is arbitrarily set to 1 deg/s. When all control drums are used in the reactivity control, there is no possibility to be constrained by the rotation limit because the differential worth is large enough to follow the power ramp rate at $\pm 10\% P_r$/min. If a smaller number of control drums were used or the required power ramp rate were faster, then the rotation rate calculated by MPC would be more likely to likely constrained. As a result, the discrepancy between the desired power trajectory and calculated power would become larger.

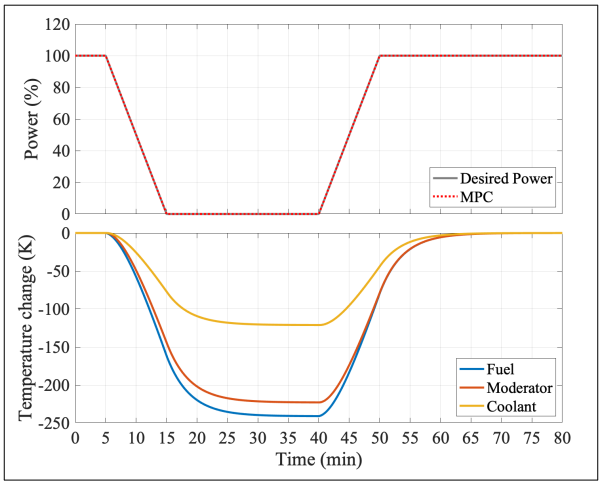

Figure 4. Power and temperature changes from initial states during load follow.

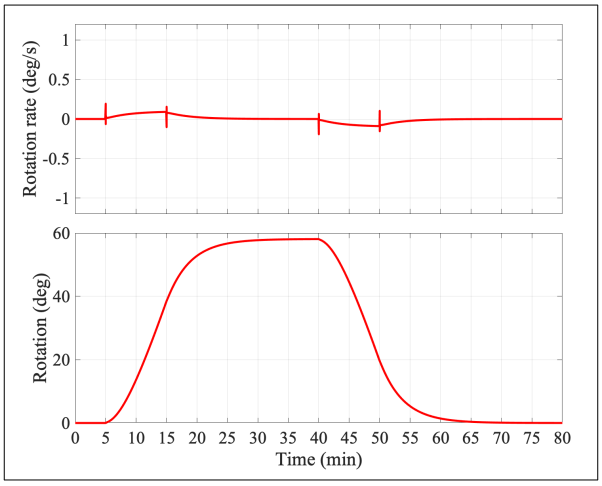

Figure 5. Control drum rotation and rotation rates during load follow.

Figure 6 presents the component of reactivities during the load follow. There are three passive temperature reactivity feedbacks through the fuel, moderator, and coolant. The reactivity feedback from both the fuel and moderator are significant. The temperature reactivity coefficients of the fuel and moderator are comparable. This is shown in Table 2, and the temperatures of both materials change significantly during the load follow maneuver. When the power is changed from 0%P_r to 100%P_r, the temperature changes of the fuel and moderator are more than 200K as shown in Fig. 4. The power level reaches 0%P_r at 15 min, and about 1000 pcm of reactivity is required up to this time. However, there are several lasting reactivity perturbations from the fuel and moderator. The additional external reactivity must be controlled by using the control drum or the other control mechanisms to compensate for these positive reactivities between 15 min and 40 min. The maximum external reactivity is -1517 pcm at 40 min. From this simulation, it is concluded that it is necessary to have ±1517 pcm of external reactivity to control the Holos reactor between 0%P_r and 100%P_r.

2.3 Summary of Reactivity Requirements

The load follow is simulated for the 7 different scenarios described in Table 1 to evaluate the required reactivity for the power maneuvers of the Holos reactor. Figure 7 presents the MPC simulation results for reactivity and power. The categories 1–3 have the same power range of 50-100%P_r, but the ramp rates are different. As shown in Figs. 7a and 7b, the required external reactivity (*i.e.,* reactivity from control drum) are similar in magnitude. **The maximum (or most negative) control drum reactivities are –758 pcm and –759 pcm for categories 1 and 2, respectively.** The required control drum reactivities immediately following the point at which 50%P_r is reached, are significantly different from each other. However, the maximum values are similar when the reactor condition is near the new equilibrium state. There will be very few situations that raise the power again within a few minutes of lowering the power. In addition, in some scenarios, there is a requirement to maintain the lowered power for hours before raising the power again [2]. Therefore, it is reasonable to determine the required reactivity after reaching equilibrium state. A similar result can be found in comparison of categories 5 (Figs. 7d and 7e). **The maximum imposed external reactivities are –1213 pcm and –1214 pcm for categories 5 and 6, respectively. The required**

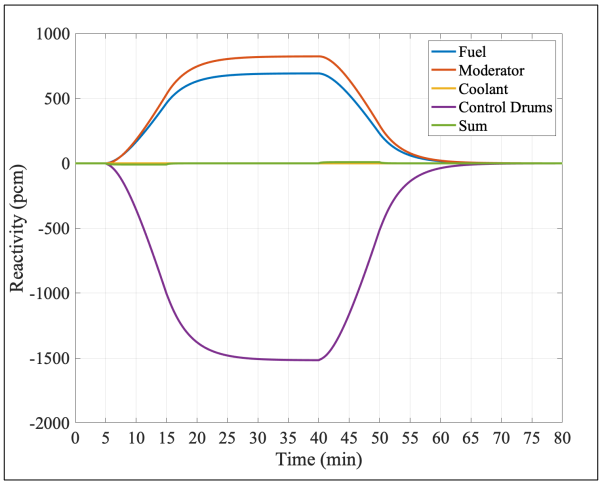

Figure 6. Reactivity change during load follow.

reactivity for category 4 in Fig. 7c is –379 pcm. The reactivity demand for category 7 is shown in Fig. 7f. The requirements on reactivity for this category are the same as the simulation scenario of Section 2.2.4. **The required reactivity to simulate category 7 is –1517 pcm.**

From these simulations, it is observed that the load follow power range is the more important parameter in determining the required reactivity. The required reactivity is nearly proportional to power change. Roughly speaking, the required reactivity can be determine by the following relation:

$$\rho_e = f_\rho \Delta P_r, \tag{46}$$

where the proportional factor f_ρ is 15.17 (Unit: pcm/%P_r), and ΔP_r is the change of power in %P_r.

A wide range of ramp rates are demonstrated in these numerical tests. The maximum ramp rate is 20%P_r/min. The control drum constrained by 1 deg/s of the maximum rotation rate shows that enough reactivity is available for FPO. The maximum rotation rate is 0.388 deg/s in the category 2 simulation. This is equivalent to 607.68 pcm/min of the imposed reactivity change rate — because the differential worth is 26.11 pcm/deg. The maximum rotation rate can be reduced depending on the tuning parameter r_w in Eq. (40). In this simulation, the tuning parameter is not used (*i.e.,* r_w=0).

3. ASSESSMENTS OF LOCAL TEMPERATURE REACTIVITY

3.1 Modeling Methodology

In order to predict the local temperature reactivity response of Holos-Quad core, Monte Carlo calculations with Serpent [11] were performed with temperature distribution obtained from the thermo-fluids code SAM [12]. Both the base SAM and Serpent models were provided by ANL. The power distribution obtained from the Serpent full core calculation is applied to single assembly SAM models to predict the individual steady-state temperature distribution for each assembly. The resulting SAM temperature distribution is then used to define the input to a full core Serpent model to obtain the base operating condition at hot full power. At Beginning of Life (BOL), Middle of Life (MOL) and End of Life (EOL) the local fuel and graphite temperature perturbations were then applied to the Serpent model to calculate the corresponding reactivity responses documented in this section.

3.1.1 Thermo-fluids calcuation with SAM

The SAM model consists of a detailed geometric model where the inner, edge and corner fluid channels are separately defined and connected to the solid structure for a full axial assembly. Figure 8 illustrates the representative assembly design. Table 3 provides some of design specifications and SAM model predictions for an average assembly. Figure 9 plots axial temperature profiles for the fuel, cladding, and matrix materials.

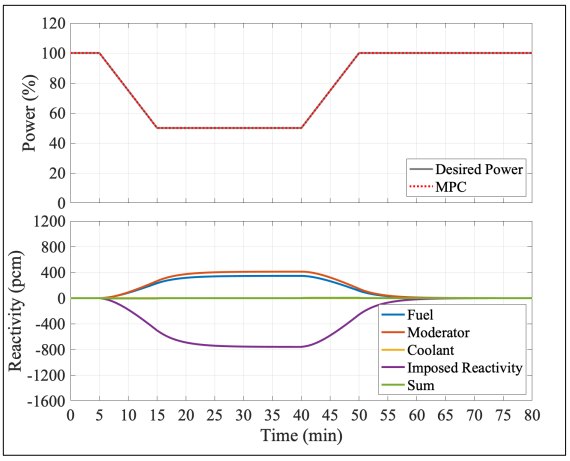

(a) Category 1 & 3: 5%P_r/min in a power range of 50-100%P_r

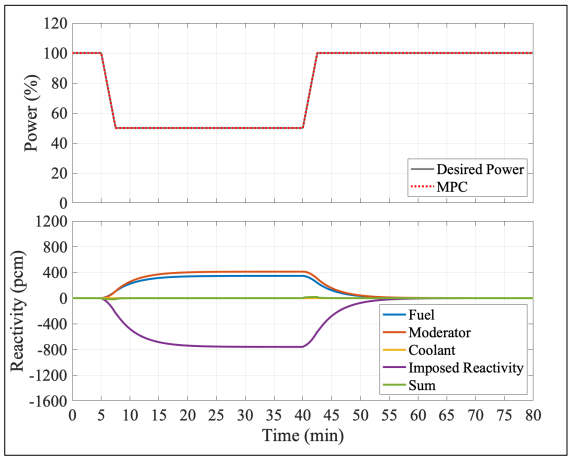

(b) Category 2: 20%P_r/min in a power range of 50-100%P_r

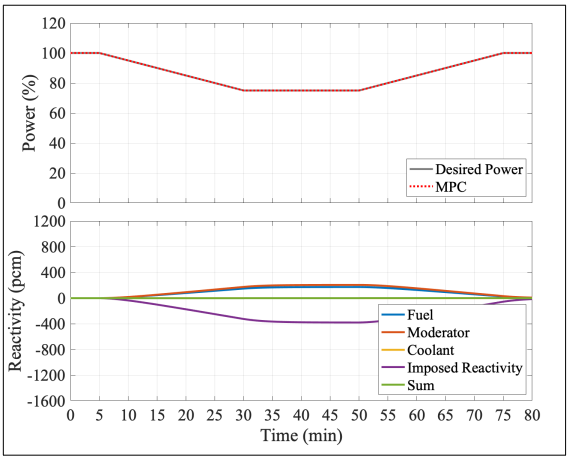

(c) Category 4: 1%P_r/min in a power range of 75-100%P_r

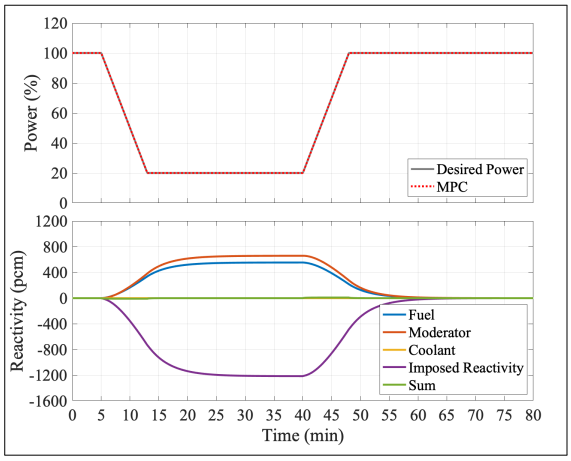

(d) Category 5: 10%P_r/min in a power range of 20-100%P_r

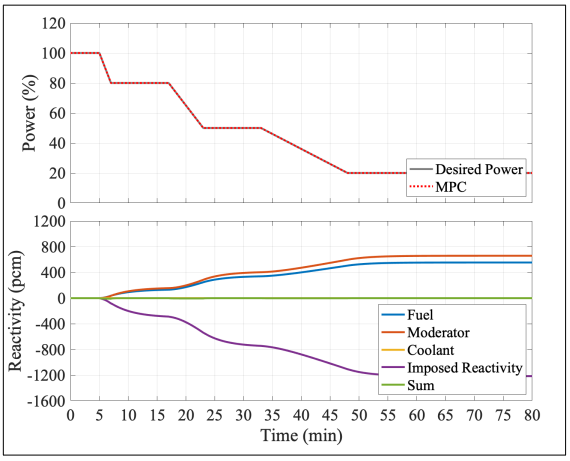

(e) Category 6: 2-10%P_r/min in a power range of 20-100%P_r

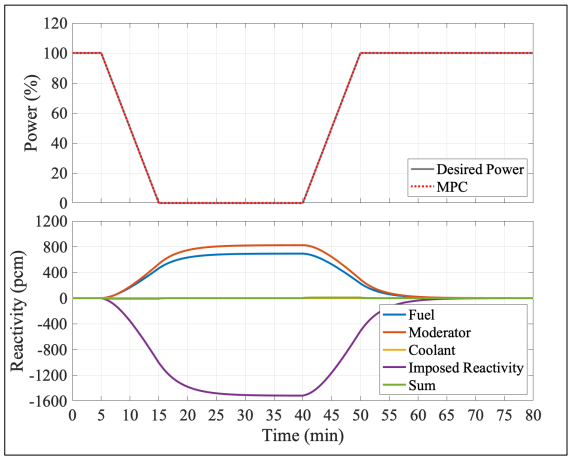

(f) Category 7: 10%P_r/min in a power range of 0-100%P_r

Figure 7. The reactivity results with different load following scenarios

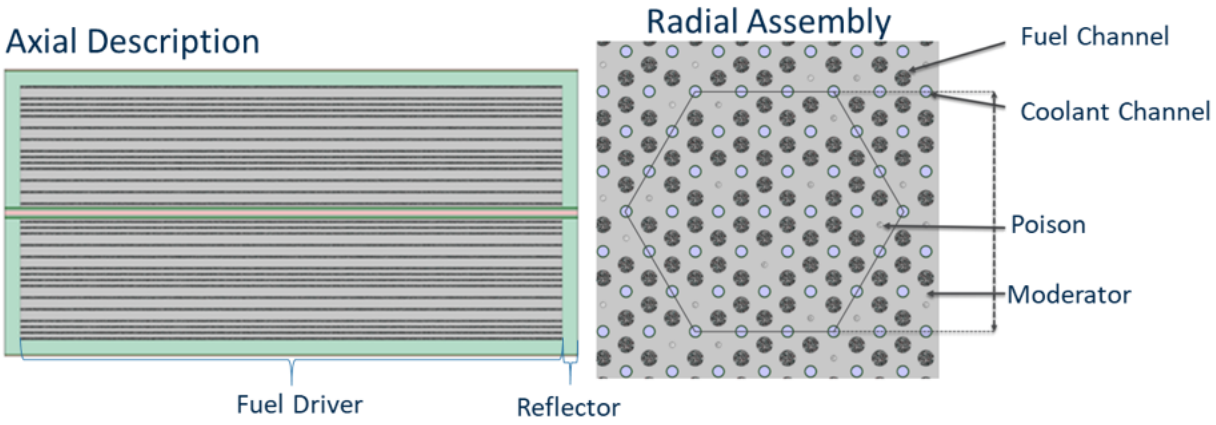

Figure 8. Illustration of Holos assembly model.

Table 3. Holos assembly parameters

Power [kW]	400
Maximum Fuel Temperature [C]	1261
Average Fuel Temperature [C]	1102
Inlet Velocity [m/s]	29.9
Pressure Drop [kPa]	7.2
Coolant Inlet Temperature [C]	590.0
Coolant Outlet Temperature [C]	849.1

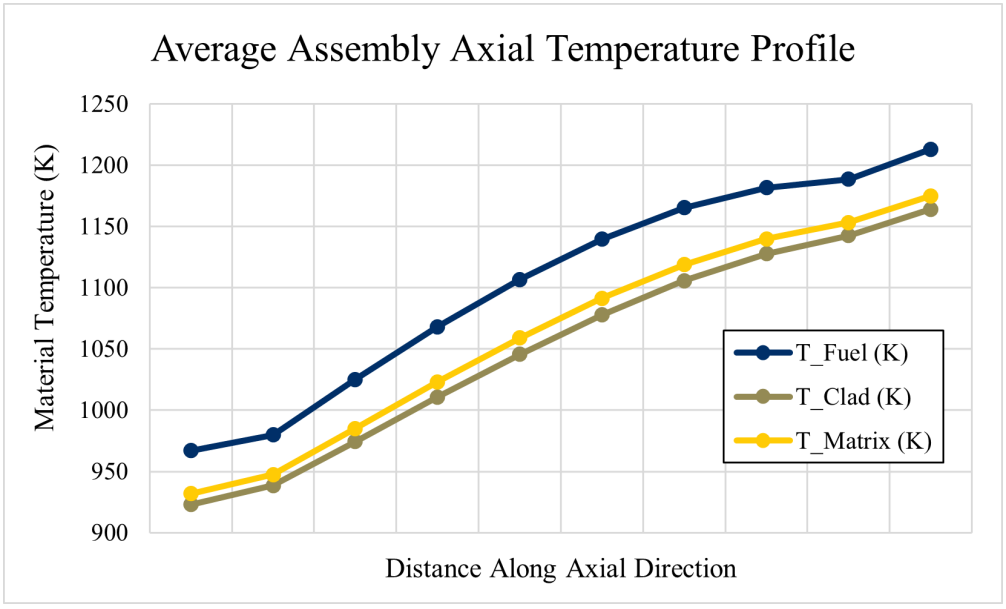

Figure 9. Average assembly axial fuel, clad, and matrix temperature.

3.1.2 Monte Carlo calculation with Serpent

The full core Serpent model contains 17 fuel assemblies (11 full, 5 half, and 1 quarter) in one of the quadrants of the core. Temperature distributions were set up for each of the 17 assemblies in one core quadrant, allowing for a more detailed understanding of the reactivity response to a perturbation in each region. The model is generated with TRISO particles that are explicitly defined and randomly positioned in each of the 10 axial and 17 radial fuel-containing sections of core. The FTC in the reactivity calculation is considered as the average temperature of the uranium kernel inside the TRISO particle for one of the 17x10 fuel regions defined in the model. The graphite temperature, or MTC, is defined as the temperature of the graphite in the TRISO coatings, matrix, and assembly graphite. All temperature perturbations are applied symmetrically and the temperature treatment for each material is accomplished by setting the temperature in the `tmp` card of Serpent. Temperature treatment of the $S(\alpha,\beta)$ thermal scattering kernel was done by using the interpolation functionality of Serpent between two predefined $S(\alpha,\beta)$ data at temperatures bounding the required temperatures. Overall, 17 radial and 10 axial regions were defined to set a temperature distribution in the Serpent model. The radial region numbering is shown in Fig. 10.

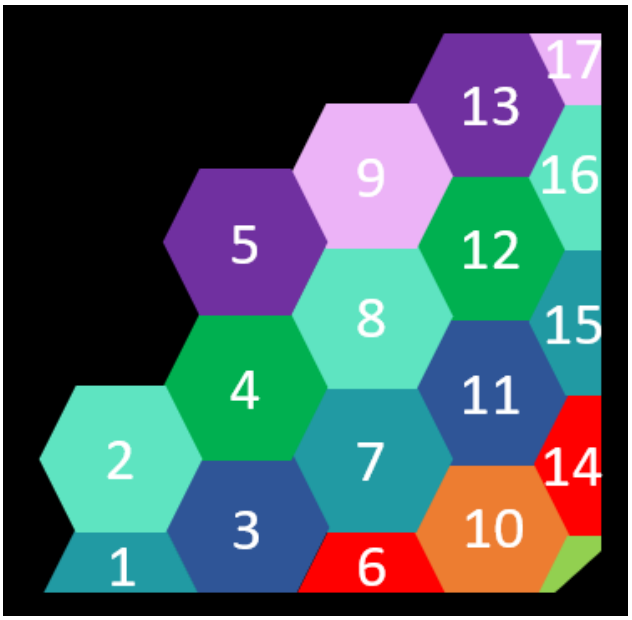

Figure 10. Block numbering for temperature reactivity coefficients

The power distribution for each radial assembly region calculated by Serpent is given in Table 4. The assembly power calculated by using the power fractions in this table was then provided as an input to the single assembly model of SAM, which used a predefined axial power profile for each radial region.

3.2 Fuel and Graphite Temperature Reactivity Results

All the Serpent calculations were performed with 200,000 neutrons per cycle, 100 inactive and 500 active cycles, which provided around 9 pcm statistical uncertainty for all calculations.

A base calculation was performed using the temperature distribution obtained from SAM. Next, a

Table 4. Serpent assembly radial power distribution

Assembly	Power Fraction
1	0.81
2	0.46
3	1.00
4	0.64
5	0.37
6	1.53
7	1.05
8	0.86
9	0.58
10	1.68
11	1.20
12	1.01
13	0.68
14	1.85
15	1.52
16	1.11
17	0.67

400 K temperature perturbation was applied independently to the fuel materials and the graphite materials in the whole core to obtain the overall fuel and graphite temperature reactivity coefficients, respectively. To obtain the local temperature reactivity response, a 400 K perturbation was independently applied to each of the fuel materials and each of the graphite materials in each of the 17 fuel regions defined in the Serpent model. While the 400 K may seem unreasonable, there were initial attempts to use smaller perturbations However, this methodology was insufficient to overcome the statistical uncertainties of the Monte Carlo transport calculations. Since the Doppler coefficient is relatively constant over a broad temperature range, and linear with respect to the square root of temperature, the larger temperature perturbation of 400 K can be justified. This approach is additionally verified in the result as the sum of the local coefficients is consistent with the whole core reactivity coefficients.

3.2.1 Beginning of life results

Tables 5 to 7 contain the FTC generated by the global and local temperature perturbations at the beginning of the core life (0 EFPY).

Table 5. Overall beginning of life temperature reactivity coefficients.

	Temperature Coefficient [pcm/K]	Temperature Coefficient per Assembly [pcm/K/assembly]
Fuel	-2.875	-0.052
Graphite	-3.696	-0.067

Table 6. Local fuel and graphite beginning of life temperature reactivity coefficients.

	Fuel Temperature Coefficient [pcm/K]	Graphite Temperature Coefficient [pcm/K]
1	-0.048	-0.037
2	-0.098	-0.129
3	-0.227	-0.241
4	-0.221	-0.183
5	-0.098	-0.107
6	-0.183	-0.217
7	-0.262	-0.260
8	-0.263	-0.210
9	-0.178	-0.212
10	-0.286	-0.556
11	-0.346	-0.328
12	-0.241	-0.241
13	-0.102	-0.144
14	-0.127	-0.324
15	-0.121	-0.226
16	-0.085	-0.160
17	-0.010	-0.043
Sum	-2.895	-3.616

Table 7. Local fuel and graphite beginning of life temperature reactivity coefficients per assembly.

	Fuel Temperature Coefficient per Assembly [pcm/K/assembly]	Graphite Temperature Coefficient per Assembly [pcm/K/assembly]
1	-0.024	-0.018
2	-0.024	-0.032
3	-0.057	-0.060
4	-0.055	-0.046
5	-0.024	-0.027
6	-0.091	-0.109
7	-0.066	-0.065
8	-0.066	-0.052
9	-0.045	-0.053
10	-0.072	-0.139
11	-0.087	-0.082
12	-0.060	-0.060
13	-0.026	-0.036
14	-0.063	-0.162
15	-0.060	-0.113
16	-0.042	-0.080
17	-0.010	-0.043
Sum	-0.871	-1.177

From Table 6, it is observed that there is up to a factor of 9 variation in the local FTC and MTC. The moderator temperature reactivity is approximately a factor of 1.3 greater than the fuel temperature coefficient at beginning of life. This effect is also approximately spatially uniform. The highest worth regions in both cases are 6, 10, and 14. Collectively, they account for about 30% of the doppler feedback. These regions are located closer to the core center where the assemblies have a higher worth and more importance to the overall core reactivity.

3.2.2 Middle of life results

Tables 8 to 10 contain the Doppler coefficients generated by the global and local temperature perturbations for a burnup of 5 FPY, representing approximately half of the life of the Holos-Quad core.

Table 8. Overall middle of life temperature reactivity coefficients.

	Temperature Coefficient [pcm/K]	Temperature Coefficient per Assembly [pcm/K/assembly]
Fuel	-2.932	-0.053
Graphite	-2.129	-0.039

Table 9. Local fuel and graphite middle of life temperature reactivity coefficients.

	Fuel Temperature Coefficient [pcm/K]	Graphite Temperature Coefficient [pcm/K]
1	-0.059	-0.047
2	-0.067	-0.047
3	-0.213	-0.185
4	-0.213	-0.143
5	-0.139	-0.139
6	-0.160	-0.049
7	-0.297	-0.174
8	-0.257	-0.144
9	-0.161	-0.140
10	-0.305	-0.290
11	-0.302	-0.185
12	-0.242	-0.142
13	-0.123	-0.110
14	-0.143	-0.176
15	-0.047	-0.137
16	-0.075	-0.054
17	-0.026	-0.011
Sum	-2.932	-2.129

Table 10. Local fuel and graphite middle of life temperature reactivity coefficients per assembly.

	Fuel Temperature Coefficient per Assembly [pcm/K/assembly]	Graphite Temperature Coefficient per Assembly [pcm/K/assembly]
1	-0.030	-0.023
2	-0.017	-0.012
3	-0.053	-0.046
4	-0.053	-0.036
5	-0.035	-0.035
6	-0.080	-0.025
7	-0.074	-0.043
8	-0.064	-0.036
9	-0.040	-0.035
10	-0.076	-0.072
11	-0.075	-0.046
12	-0.060	-0.035
13	-0.031	-0.027
14	-0.071	-0.088
15	-0.023	-0.068
16	-0.038	-0.027
17	-0.026	-0.011
Sum	-0.847	-0.667

3.2.3 End of life results

Tables 11 to 13 contain the Doppler coefficients generated by the global and local temperature perturbations for a burnup of 10 FPY, representing approximately the full life of the Holos-Quad core.

Table 11. Overall end of life temperature reactivity coefficients.

	Temperature Coefficient [pcm/K]	Temperature Coefficient per Assembly [pcm/K/assembly]
Fuel	-3.206	-0.058
Graphite	-2.818	-0.051

Table 12. Local fuel and graphite end of life temperature reactivity coefficients.

	Fuel Temperature Coefficient [pcm/K]	Graphite Temperature Coefficient [pcm/K]
1	-0.017	-0.038
2	-0.067	-0.086
3	-0.210	-0.181
4	-0.191	-0.164
5	-0.107	-0.149
6	-0.188	-0.104
7	-0.336	-0.266
8	-0.276	-0.214
9	-0.133	-0.133
10	-0.364	-0.394
11	-0.368	-0.319
12	-0.257	-0.219
13	-0.079	-0.099
14	-0.149	-0.177
15	-0.139	-0.133
16	-0.095	-0.058
17	-0.004	-0.015
Sum	-2.981	-2.749

Table 13. Local fuel and graphite end of life temperature reactivity coefficients per assembly.

	Fuel Temperature Coefficient per Assembly [pcm/K/assembly]	Graphite Temperature Coefficient per Assembly [pcm/K/assembly]
1	-0.009	-0.019
2	-0.017	-0.022
3	-0.053	-0.045
4	-0.048	-0.041
5	-0.027	-0.037
6	-0.094	-0.052
7	-0.084	-0.067
8	-0.069	-0.053
9	-0.033	-0.033
10	-0.091	-0.099
11	-0.092	-0.080
12	-0.064	-0.055
13	-0.020	-0.025
14	-0.074	-0.089
15	-0.020	-0.066
16	-0.048	-0.029
17	-0.004	-0.015
Sum	-0.895	-0.826

3.2.4 Comparing results at different burnups

Figures 11 and 12 compare the FTC and MTC, respectively, for different burnups.

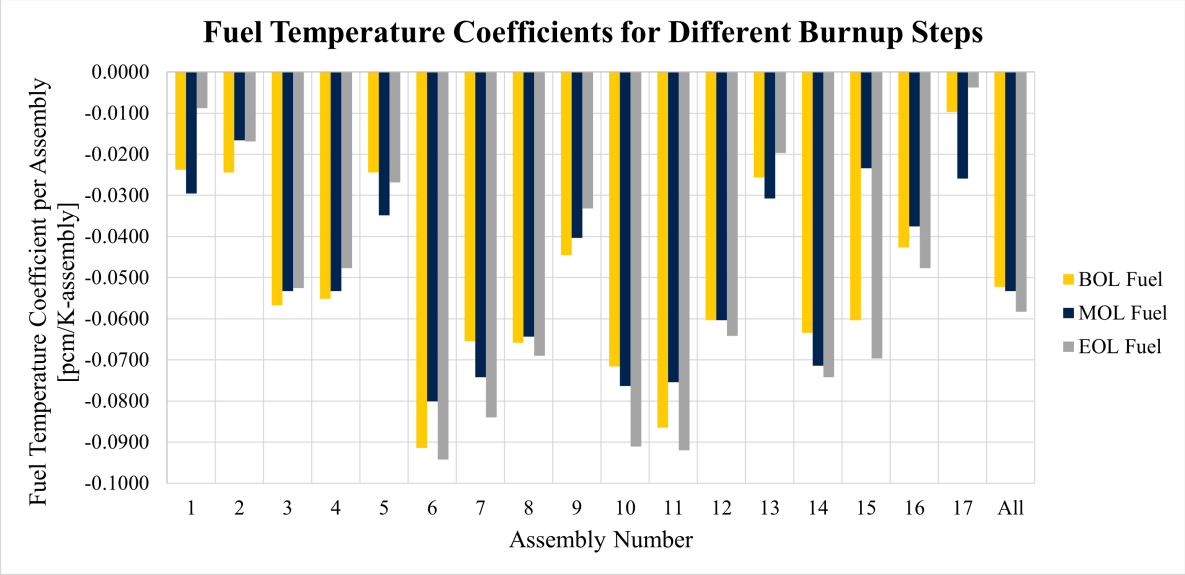

Figure 11. FTC per assembly for each assembly at different burnups.

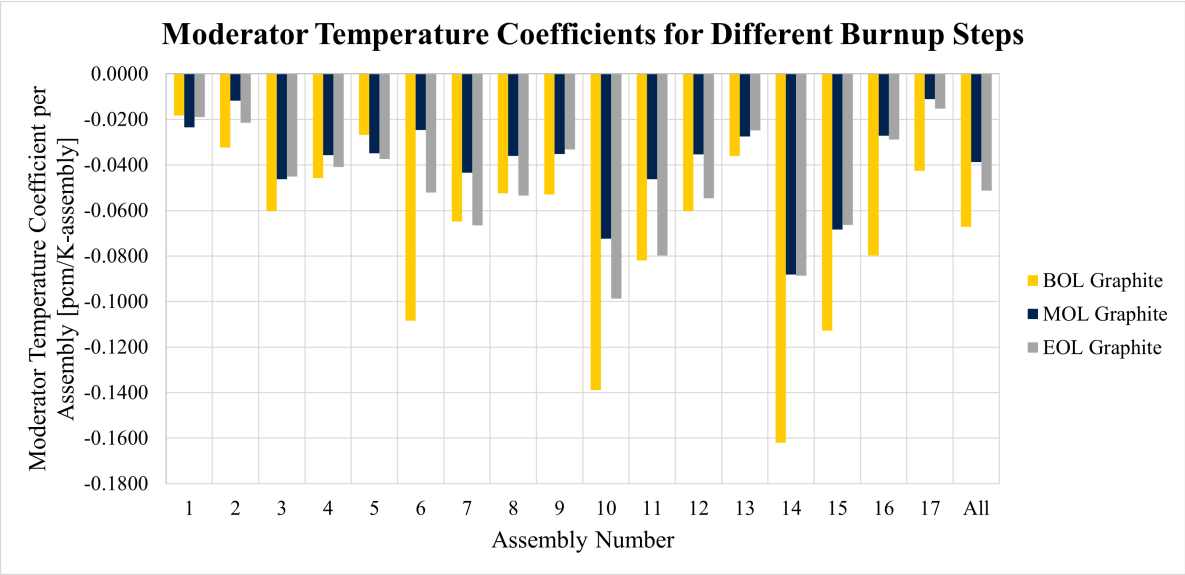

Figure 12. MTC per assembly for each assembly at different burnups.

As shown in the above figures, the temperature coefficients for the fuel and moderator vary with burnup. The coefficients changes substantially in some cases with burnup because, as the fuel is burned, ^{235}U, Pu and fission products are built up changing the local neutron spectrum due to the addition of more resonance absorbers. The additional resonance absorbers cause the FTC to become more negative at the MOL and EOL. Most local changes in the Doppler reactivity are not very significant, but some assemblies have significant variation for different burnups.

Generally, the FTCs are more consistent for different burnups, and the MTCs change much more substantially. This occurs because the graphite temperature coefficient is strongly dependent on the thermal neutron spectrum, which, in the case of HTRs, has significant spatial variation in high leakage cores like microreactors. This causes obvious local swings in the temperature coefficient of the graphite at BOL, MOL, and EOL.

4. ASSESSMENT OF CONTROL DRUM/REFLECTOR REACTIVITY

Similar to worth curves assessment of control rods in LWRs, reactivity assessment of the control drums is of high importance in the design process of reactor control system. The details of the reactivity worth curves are very useful in the safe operation of the reactor–and would be essential under automation. The curves can be used to improve the control system predictions by integrating them in a physics-based control model such as MPC, as described in Section 2.2.4. In this aspect, deriving analytic expressions holds significant advantages over numerical methods. Such expression can be derived based on first order perturbation theory, as described below.

In Section 4.1 the Monte Carlo modelling is presented. First order perturbation theory is described in Section 4.2.1, followed by derivations of two analytic expressions: simple (Section 4.2.2) and improved (Section 4.2.3). Section 4.2.4 also presents an alternative approach, namely using a Fourier series expansion to find the harmonic coefficients of the drum reactivity worth curves. Finally, the results are shown in Section 4.2.5.

4.1 Monte Carlo Modeling

Assessment of control drum reactivity was carried using the Monte Carlo code Serpent, as described in Section 3.1. The calculations used ENDF-B7.1 nuclear data with materials at operating conditions. The extent of the core model included explicit treatment of all core structures and components out to the ISO container boundary. The majority of the simulations were run with 100 inactive cycles, 500 total cycles, and 100,000 particles per cycle to reduce run times. This resulted in uncertainties of 10 pcm to 15 pcm in k_{eff} . Some cases used more particles for reduced uncertainties. The models used here are the sme base models as those presented in Section 3

The base models were provided by ANL and modified to allow each control drum to be rotated independently. These models were used to calculate integral and differential control drum worth curves for 12 different drum patterns using drum rotation increments of 10° . The 12 drum patterns are shown in Fig. 13. These 12 patterns effectively cover each unique combination of drums as the even and odd drums have slightly different local geometries, and are not exactly equivalent. The patterns also include some that are highly asymmetric.

Due to the proprietary nature of the reactor design, no further details of the models are given. However, detailed geometric, material, and other design parameters can be provided with a direct request to HolosGen.

The results presented below include proper uncertainty propagation of k_{eff} to the reactivity ρ. Further details about uncertainty propagation for reactivity are found in the previous report [4]. Compared to the results previously published in [4], some minor enhancements were made to these models to fix some mistakes and improve the overall statistics.

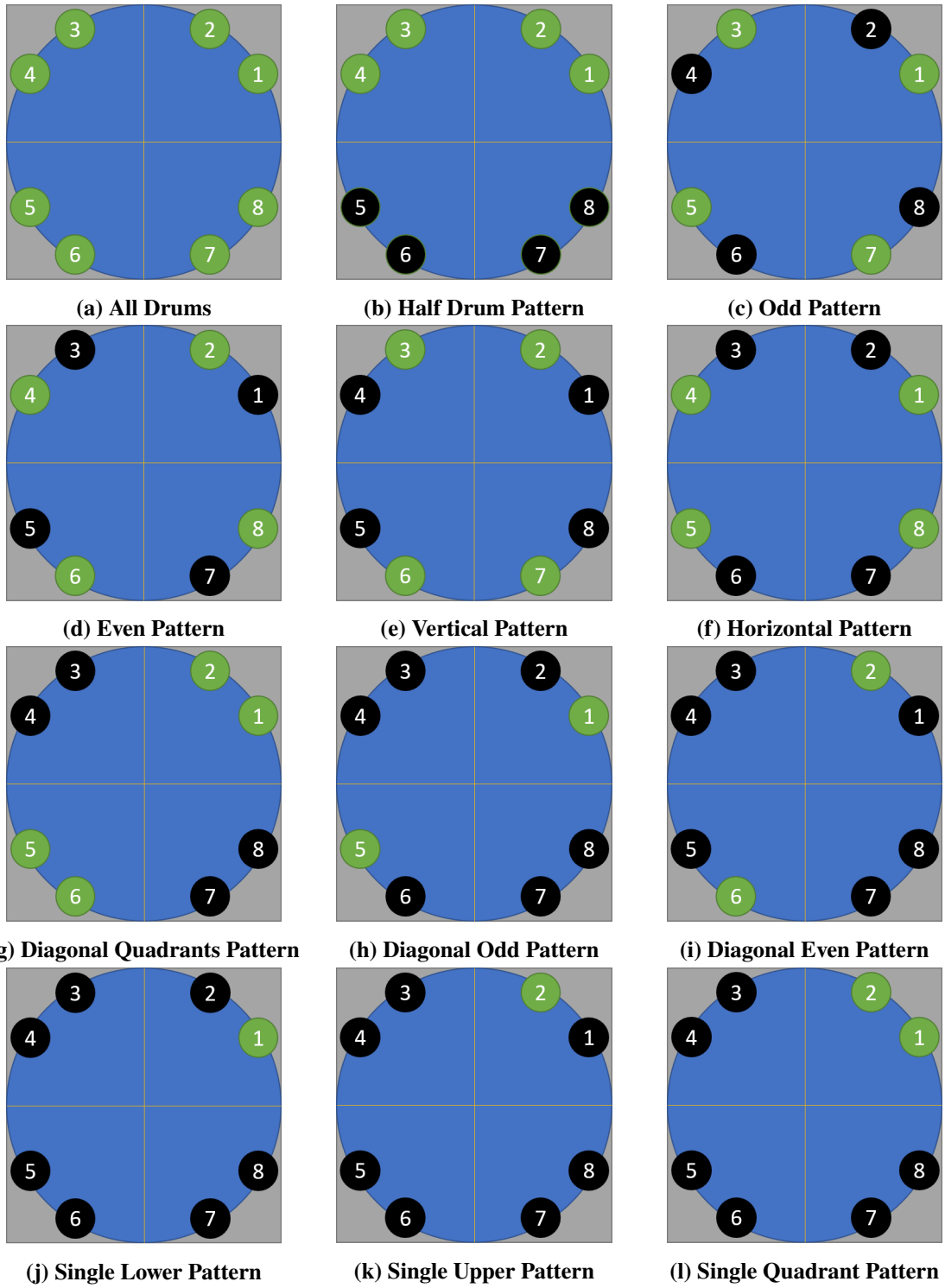

Figure 13. Control Drum Patterns (green indicates the drums that are rotated symmetrically for the given pattern; black are drums rotated out)

4.1.1 Numerical Results

The integral and differential worth curves computed from the Monte Carlo models are presented in Figs. 14 and 15, respectively. In these figures, the Monte Carlo results are depicted against the simple analytic expression, derived in Section 4.2.2.

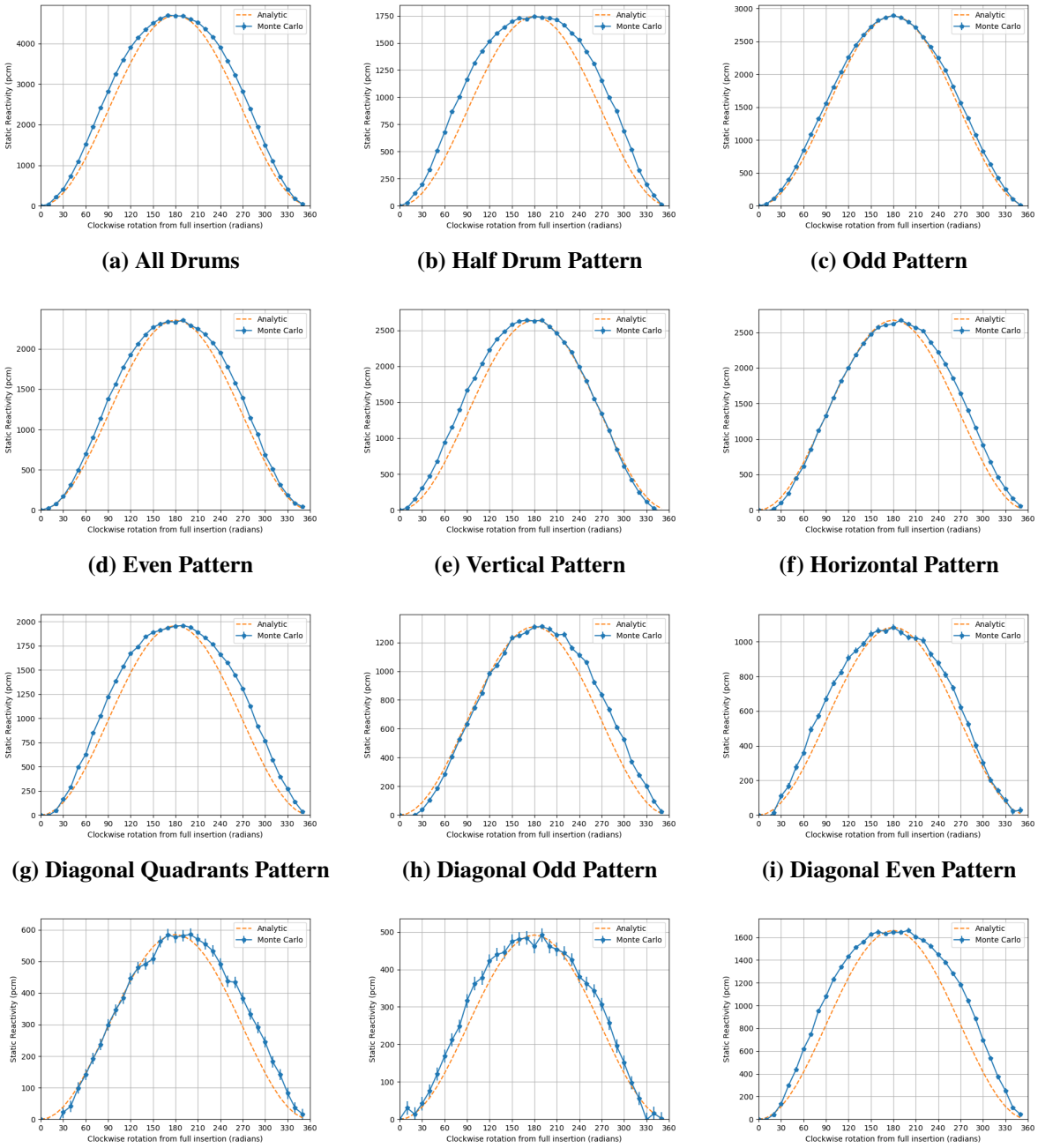

(a) All Drums **(b) Half Drum Pattern** **(c) Odd Pattern**

(d) Even Pattern **(e) Vertical Pattern** **(f) Horizontal Pattern**

(g) Diagonal Quadrants Pattern **(h) Diagonal Odd Pattern** **(i) Diagonal Even Pattern**

(j) Single Lower Pattern **(k) Single Upper Pattern** **(l) Single Quadrant Pattern**

Figure 14. Integral Control Drum Reactivity Worths

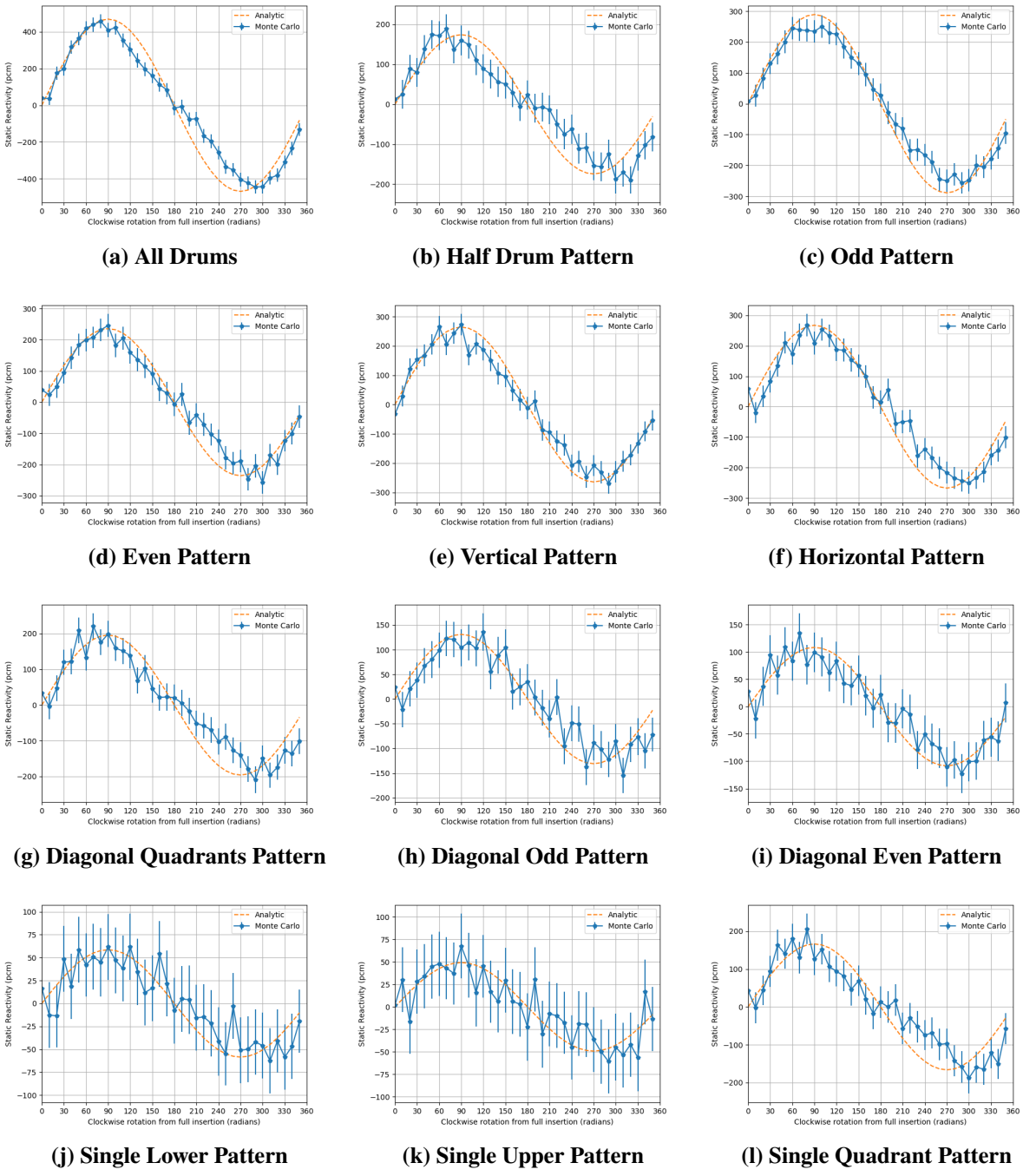

(a) All Drums **(b) Half Drum Pattern** **(c) Odd Pattern**

(d) Even Pattern **(e) Vertical Pattern** **(f) Horizontal Pattern**

(g) Diagonal Quadrants Pattern **(h) Diagonal Odd Pattern** **(i) Diagonal Even Pattern**

(j) Single Lower Pattern **(k) Single Upper Pattern** **(l) Single Quadrant Pattern**

Figure 15. Differential Control Drum Reactivity Worths

Several observations are made from the examination of Fig. 14. In all cases the integral drum worth curve is generally shaped in the form of a sine or cosine. Similarly, for the Fig. 15, the derivatives would consistent with integral drum worths being represented by a sine or cosine. Therefore, we suggest that the differential drum worths are merely a different way of viewing the same data. One note about viewing the differential drum worths is that the statistical uncertainty is relatively greater–due to the differential worth being smaller. Another observation is that there are clear

systematic deviations from the analytic model. This suggests that other analytical models more complex than that derived in Section 4.2.2 be investigated. This is the focus of Section 4.2.

The last point of analysis of the Monte Carlo results is to note that different whole core symmetric drum patterns involving differing numbers of drums provide scaled worth curves. This is illustrated by Fig. 16. This aspect of the reactor design provides a nice "menu" of drum patterns from which to control the reactor under various conditions, and its likely this can be used advantageously in a multiple input, multiple output control strategy to maximize operational life, optimize xenon oscillations, or optimize margin to Thermal Hydraulics/Fluids (TH) limits. Topics such as these will be the focus of the next milestone of the project.

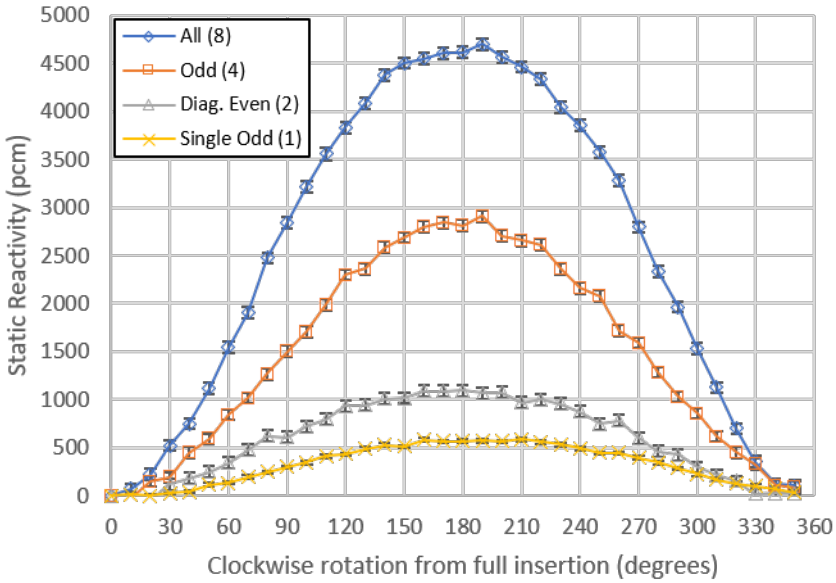

Figure 16. Comparisons of Integral Drum Worths for Different Patterns

4.2 Analytic Models

In the previous section (Section 4.1, many expensive Monte Carlo calculations were run (totaling ~64,8000 cpu-hours) to quantify the reactivity worth curves. In this section we use this data to develop a series of much simpler expressions with increasing complexity and accuracy to approximate the data produced from the Monte Carlo calculations. These models would be necessary for use in model or state-space based control algorithms to ensure sufficient accuracy. Additionally, their forms may be used generally in the design of other microreactor designs having rotating control drums. This section proceeds with first arriving at an expression of the reactivity based on first order perturbation theory. Then several models are considered for to representation the perturbation of the reflector cross section by the control drum.

4.2.1 First Order Perturbation Theory

First order perturbation theory has long been a useful tool in reactor physics. In this subsection we briefly review some of the fundamental equations and associated assumptions to arrive at simple expressions for the reactivity. The resulting equations will then be used to develop simplified

analytical expressions for the control drum reactivity worth curves.

We begin with the equation for reactivity using first order perturbation theory. The derivation of which is readily found in nuclear engineering textbooks [13].

$$\rho = \frac{\delta k}{k} = \frac{\left\langle \phi^*, \left(\frac{1}{k}\boldsymbol{\delta F} - \boldsymbol{\delta M}\right)\phi \right\rangle}{\frac{1}{k}\left\langle \phi^*, \boldsymbol{\delta F}\phi \right\rangle}, \tag{47}$$

here δk, $\boldsymbol{\delta F}$, and $\boldsymbol{\delta M}$ are the perturbations to the multiplication factor, fission operator, and migration and loss operator, respectively. The scalar flux is denoted by ϕ and its adjoint, ϕ^*. The fission operator, $\boldsymbol{F}$, and migration-loss operator, $\boldsymbol{M}$, simply satisfy the neutron balance equation and can generally represent transport or diffusion and multigroup or continuous energy forms. The main approximation of first order perturbation theory is to assume that the perturbed scalar flux is well represented by the unperturbed scalar flux in both space and energy. This is generally true for small perturbations. It follows naturally that perturbations to the reactor that do not induce strong spectral changes or changes to the shape of the scalar flux are well represented by first order perturbation theory.

We consider now the justification of this assumption to microreactors and insist that for perturbations to temperature that are global and uniform, or for perturbations to the radial reflector composition or leakage rate are likely to be well represented by first order perturbation theory. As we will see in Section 4.2.5 this is true in many, but not all, cases for perturbations to the reflector.

Next we wish to further simplify Eq. (47) by simplifying the operators $\boldsymbol{\delta F}$, and $\boldsymbol{\delta M}$. For these operators we assume one-speed diffusion so that they may be written explicitly as:

$$\boldsymbol{\delta M} = -\nabla \cdot \delta D \nabla + \delta \Sigma_a, \tag{48a}$$

$$\boldsymbol{\delta F} = \delta(\nu \Sigma_f), \tag{48b}$$

where δD, $\delta \Sigma_a$, and $\delta(\nu\Sigma_f)$ are the perturbations to the diffusion coefficient, absorption cross section, and fission production cross section, respectively. Substituting Eq. (48) into Eq. (47) yields:

$$\rho = \frac{\int_V \phi^* \left[\frac{1}{k}\delta\left(\nu\Sigma_f\right)\phi + \nabla \cdot \delta D \nabla \phi - \delta \Sigma_a \phi\right] dV}{\frac{1}{k}\int_V \nu\Sigma_f \phi^* \phi dV}. \tag{49}$$

Further, recalling that the one-speed diffusion equation is self-adjoint leads to:

$$\rho = \frac{\int_V \frac{1}{k}\delta\left(\nu\Sigma_f\right)\phi^2 + \nabla \cdot \delta D \nabla \phi^2 - \delta \Sigma_a \phi^2 dV}{\frac{1}{k}\int_V \nu\Sigma_f \phi^2 dV}. \tag{50}$$

The one-speed assumption is reasonable so long as accurate energy integrated effective cross sections (and their perturbations) can be obtained. Moreover, the conditions under which we make the assumptions regarding the accuracy of first order perturbation theory allow us to confidently assume one-speed. The one-speed assumption will break down if perturbations to the system cause non-trivial spectral or shape changes in the scalar flux. Since have assumed this to be the case for first order perturbation theory, it applies equally usefully to one-speed diffusion. Perturbations

to the diffusion coefficient or leakage, may be invalidate the assumption of diffusion since this is already questionable at the system boundary. However, our goal is to apply this theory to derive analytical expressions for the control drum worth, which we may reasonably assume do not cause perturbations to the diffusion coefficient.

From the equation for the reactivity based on one-speed diffusion and first order perturbation theory, we further simplify Eq. (50) for the case of control drum movement. Specifically, we observe that perturbations induced by rotation of the control drums:

- do not cause perturbations to the fission cross section ($\delta(\nu\Sigma_f) = 0$)
- cause much larger perturbations in the absorption cross section than the diffusion coefficient ($\delta D << \delta\Sigma_a$), therefore we may neglect the perturbation to the diffusion coefficient ($\delta D \approxeq 0$).

Applying these assumptions to Eq. (50) yields:

$$\rho = \frac{\int_V -\delta\Sigma_a \phi^2 dV}{\frac{1}{k}\int_V \nu\Sigma_f \phi^2 dV} \tag{51}$$

If we further assume that the fission cross section, and perturbation to the absorption are uniform, then the integrals of the scalar flux cancel and we obtain:

$$\rho = \frac{-\delta\Sigma_a}{\Sigma_a + DB^2}. \tag{52}$$

Note this equation has been further simplified by the one-speed diffusion expression for k. The next task at hand is to now derive, or rather develop by inference, a more explicit expression for $\delta\Sigma_a$. This will be described in the next two sections.

4.2.2 Simple Physical Model

We note that the uniformity of the coefficients, following the first order perturbation theory, is quite similar to assuming a point reactor (although there are subtle differences). Conceiving of the problem as a point reactor and a control drum, we may conceptualize this problem in the way illustrated by Fig. 17.

Considering the "physics" of Fig. 17, we expect the absorption cross section (and reactivity–since it is proportional to $\delta\Sigma_a$) should vary in the following way, if the fully rotated in position is taken as the reference position (i.e. 0°).

- the maximum reactivity should occur at 180°
- the reactivity will increase when rotating from 0° to 180°
- rotating the drum further from 180° to 360° will cause the reactivity decrease
- the increase in reactivity from 0° to 180° should be symmetric to the decrease in reactivity from 180° to 360° .

Basic trigonometry informs us that the underlying function should be the sin or cos. An analogous problem to illustrate this would be the equation for the distance between a point next to a circle and a point on the edge of the circle as function of the rotational position of the circle.

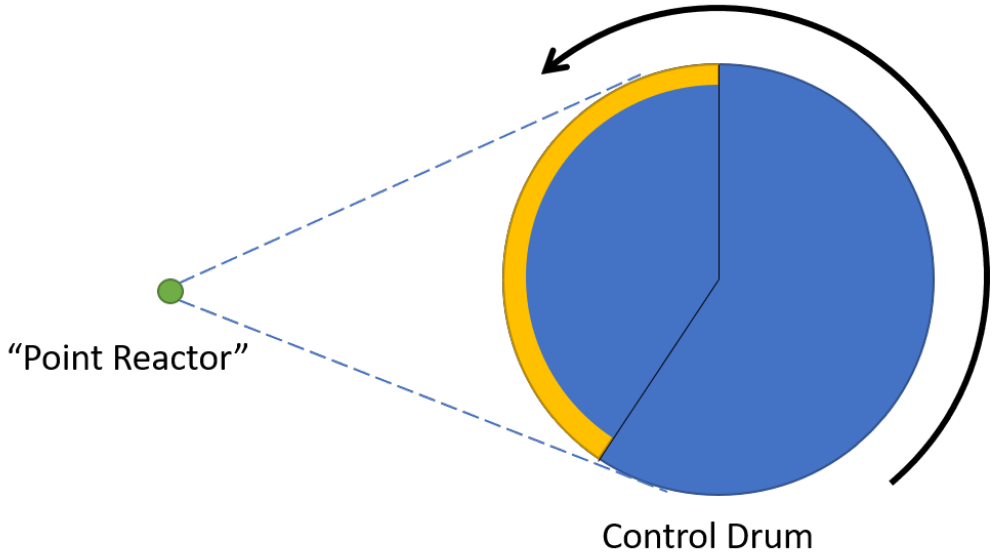

Figure 17. Point Reactor and Rotating Control Drum

The general form of the sine function can be expressed as:

$$f(\theta) = A \sin\left(\frac{\theta}{\lambda} + \omega\right) + K, \tag{53}$$

where A is the amplitude, K is the vertical shift, λ is the period, and ω is the phase shift. From our previous statements regarding the expectations of the reactivity (specifically it is the integral reactivity), the period, λ, should be 1. Since the minimum reactivity value should occur at 0° , and the maximum at 180° , this implies a phase shift of −90° (or +270°). Because the sine function is bounded on the interval $[-1, 1]$, and from our above statements we desire the reactivity to exist on $[0, \rho_{\max}]$, this implies that $K = A$ and $A = \rho_{\max}/2$. We may now write explicitly, an equation for the integral reactivity worth:

$$\boxed{\rho(\theta) = \frac{\rho_{\max}}{2}\left(1 - \cos\theta\right)}, \tag{54}$$

where $\rho_{\max}$ is:

$$\rho_{\max} = \frac{1}{k_{\text{drums out}}} - \frac{1}{k_{\text{drums in}}}. \tag{55}$$

Note that to obtain the form of Eq. (54) we have made use of the trigonometric identity $-\cos x = \sin x - \frac{\pi}{2}$. The differential control drum worth is readily obtained through differentiation of Eq. (54).

$$\boxed{\frac{d\rho(\theta)}{d\theta} = \frac{\rho_{\max}}{2}\sin\theta}, \tag{56}$$

The accuracy of this model can be qualitatively assessed in Fig. 14, and quantitatively assessed in Fig. 25. From Fig. 14 it can be reasonably observed that the model does well in some cases and quite poorly in others. From Fig. 25 it is much more obvious how poorly this simple model is at

representing the reactivitiy worth curves for some patterns. In some sense, this is to be expected given the assumptions and simplifications that led to its derivation. Consequently, this comparison motivates developing more complex models that are the focus of Sections 4.2.3 and 4.2.4, and that this simple model may only have utility for its pedagogical value.

4.2.3 Improved Physical Model

To improve the accuracy of the simple model, we consider a conceptually different problem from which to derive our expression for $\Delta\Sigma_a$. Instead of treating the reactor and drum as points, we assume a cylindrical drum of radius R, where the absorber is covering a coating angle of 2α. We also assume that the drum is located next to an infinite slab reactor, with a constant, mono-energetic, mono-directional neutron flux emitted in the negative x direction. A cross section of the drum in the $X-Y$ plane is depicted in Fig. 18.

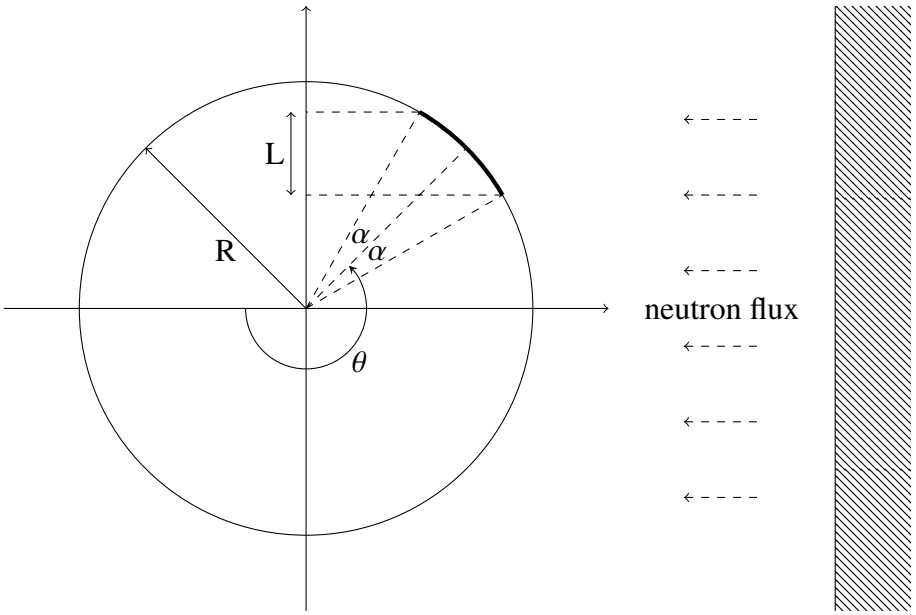

Figure 18. Diagram of a control drum with coating angle 2α and a rotating angle θ next to an infinite slab source.

The rotation of the drum is represented by θ, measured from $-\hat{x}$ and counter-clockwise to the middle of the absorber angle. For simplicity, in this section we use radians instead of degrees as the angular unit. By this definition, $\theta = 0$ and $\theta = \pi$ represent control drum rotated fully out and fully in, respectively.

Since the neutron flux is directed in $-\hat{x}$, the absorption, and hence the reactivity, are proportional to the projection of the absorbing arch on the y axis. Let us define this absorption length as L. It

can be shown that the dependence of L on the coating and rotation angles is:

$$L(\alpha,\theta) = \begin{cases} 0 \ , & 0 < \theta < \frac{\pi}{2} - \alpha \\ -R\left(\sin(\alpha+\theta) - 1\right) \ , & \frac{\pi}{2} - \alpha < \theta < \frac{\pi}{2} + \alpha \\ -R\left(\sin(\alpha+\theta) + \sin(\alpha-\theta)\right) \ , & \frac{\pi}{2} + \alpha < \theta < \frac{3\pi}{2} - \alpha \\ -R\left(\sin(\alpha-\theta) - 1\right) \ , & \frac{3\pi}{2} - \alpha < \theta < \frac{3\pi}{2} + \alpha \\ 0 \ , & \frac{3\pi}{2} + \alpha < \theta < 2\pi \end{cases} \tag{57}$$

It can be shown that this function is continuous and differentiable for all θ values. In the special case of $\alpha = \pi/2$, i.e. absorbing arch is covering half the drum perimeter, the expression simplifies to:

$$L(\theta) = R\left(1 - \cos\theta\right) \tag{58}$$

for $0 < \theta < 2\pi$. This expression is identical to Eq. (54), assuming a correlation between the radius of the drum (R) and the maximal reactivity (ρ_{max}). In Fig. 19 the normalized absorption length L is plotted against the rotating angle θ for several coating angles.

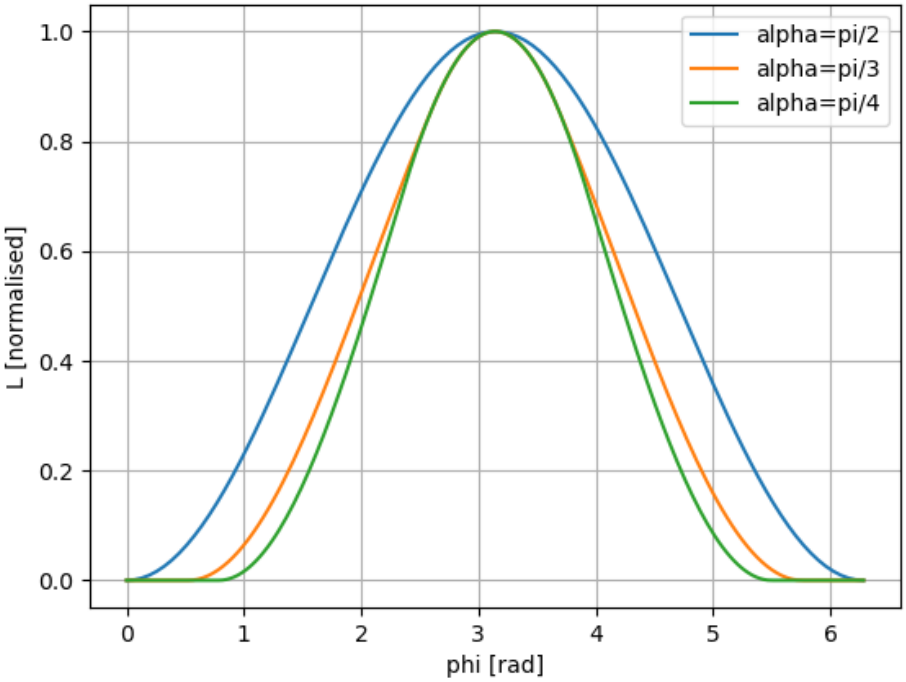

Figure 19. Absorption length (L) dependence on rotation angle (θ) for various coating angles.

In the above we assumed a uniform mono-directional flux. It yields a symmetric curve (with respect to π), as depicted in Fig. 19. However, the existence of a neighboring drum or other local heterogeneities that exist in the real design, can change the flux shape locally, yielding non-symmetric behavior. To account for this phenomenon, a correction factor f is introduced– multiplying the absorption length L.

To consider the asymmetric case, we assume a neighboring drum (drum 2) next to the analyzed drum (drum 1), as depicted in Fig. 20. We assume that drum 2 is modifying the flux shape around it in a $1/r^2$ manner, as illustrated by the concentric dashed circles around it. As a result, a quadratic correction factor is required. This is depicted by the parabolic dashed curve in Fig. 20:

$$f = a\theta^2 + b\theta + c \tag{59}$$

We require that the minimum of this function is equal to 1, and that it occurs at an angle θ_0, which

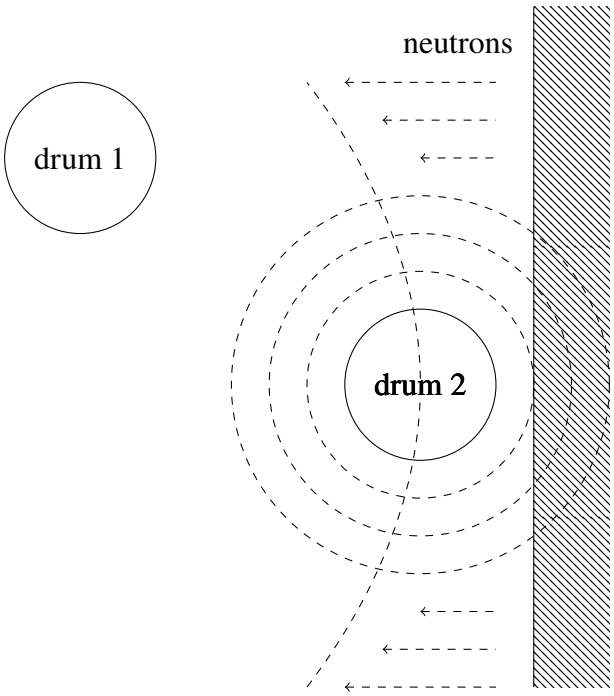

Figure 20. Diagram of a neighboring drum, introducing a parabolic correction factor to the absorption spatial dependence.

depends on the location of drum 2 relative to drum 1. From this two following conditions are obtained: $b = -2a\theta_0$ and $c = 1 + a\theta_0^2$. In the case of a coating angle of π, the reactivity takes the form:

$$\rho(\theta) = \rho_{max}(1 - \cos\theta)(a\theta^2 + b\theta + c) \tag{60}$$

where b and c depend on the parameters a and θ_0 as described above. These parameters can be found by fitting the curve using a linear regression. More generally, they may be obtained analytically or by just a few Monte Carlo calculations–rather than 36. In Fig. 21 the quadratic correction factor is shown for several values of θ_0, and for a given value of a.

4.2.4 Fourier Series Expansion

The last method developed was to use a Fourier series expansion where the coefficients are obtained through a least-squares regression of the Monte Carlo results. Since the worth curves are even functions, we use only even functions (cosine) in the expansion:

$$\rho(\theta) = a_0 + \sum_{n=1}^{N} a_i \cos(n\theta) \tag{61}$$

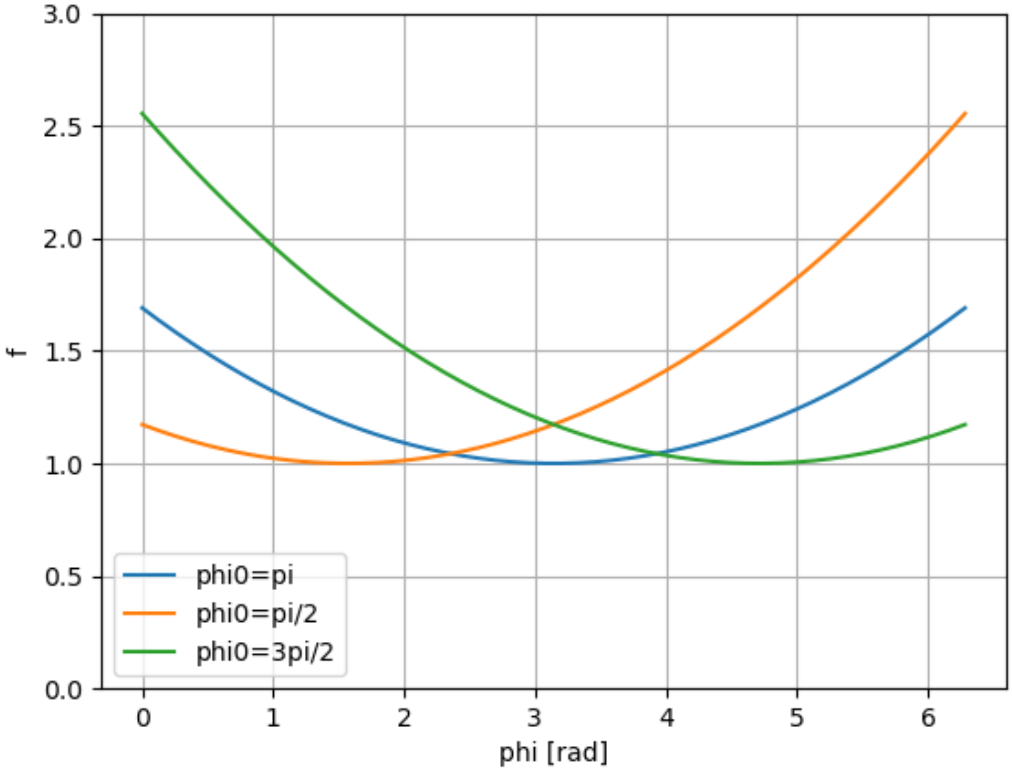

Figure 21. Quadratic correction factor for various values of θ_0.

We studied the dependence of the accuracy of the fit on the expansion order (N) by analyzing the coefficient of determination (R^2). The results are depicted in Fig. 22. It is seen that for all cases, the second order ($N = 2$) improves the fit significantly, while higher orders ($N \geq 3$) have negligible contribution. Therefore, in the following we use a second order expansion for all cases. In Fig. 23, the coefficients of the second-order expansion are plotted for all of the cases. For simplicity, the raw reactivity was normalized (divided by ρ_{max} for all of the cases, such that the series coefficients will have similar magnitude. It is seen that while a_0 and a_1 do not vary significantly between the cases ($\sim$ 10%), the value of a_2 does vary significantly (up to $\sim$ 100%). This suggests that pattern dependent coefficients for a_2 would be needed, but average coefficients for a_0 and a_1 should be able to provide suitable accuracy. For this model, the prospect of deriving coefficients (rather than fitting them) is a bit more challenging than in the previous analytic models, but ultimately we assume its possible and it will be considered in future work.

4.2.5 Results and Analysis

In all of the cases, both the improved physical model an the Fourier series expansion provide better agreement with the Monte Carlo results compared to the simple model previously derived in [4]. An example is shown in Fig. 24 for the case of horizontal pattern.

As a quantitative measure of the accuracy of the models, $\rho(\theta_i)$, to Monte Carlo result, $\rho_{\mathrm{MC,i}}$, we

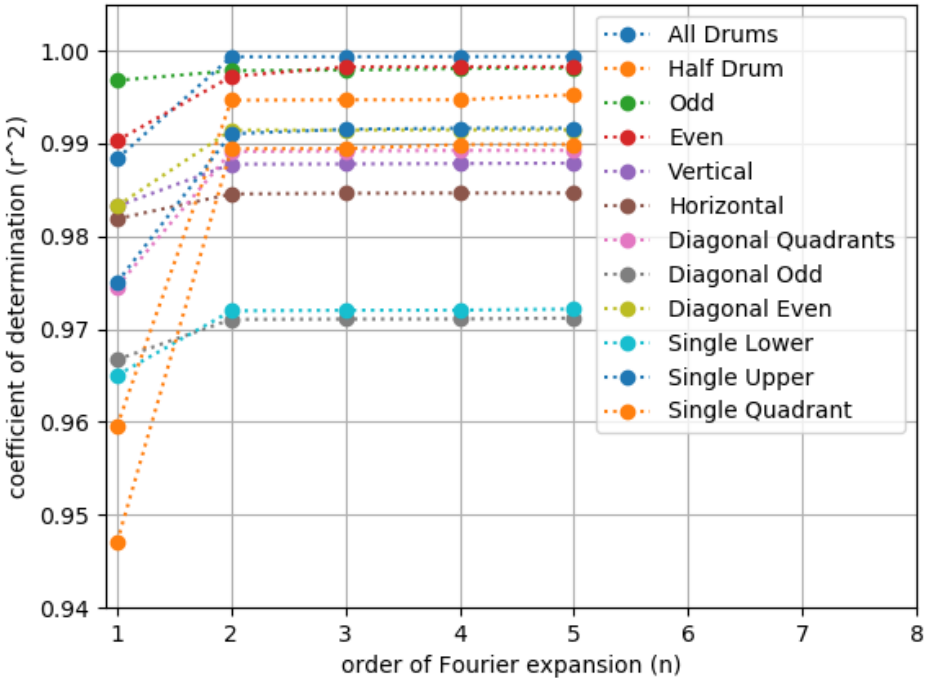

Figure 22. Dependence of coefficient of determination (R^2) on Fourier expansion order (N).

use the following root mean square difference in reactivity.

$$\text{RMS} = \sqrt{\frac{1}{N}\sum_{i}^{N}\left(\rho(\theta_i) - \rho_{\text{MC,i}}\right)^2} \tag{62}$$

We compare this to an RMS of the Monte Carlo uncertainty,

$$\sigma_{\text{RMS}} = \sqrt{\frac{1}{N}\sum_{i}^{N}\sigma_{\rho,i}^2} \tag{63}$$

and suggest that if the ratio is less 2, then "on average" Eq. (54) is predicting a reactivity worth within 2σ of the Monte Carlo uncertainty. The ratio for all three methods is presented in Fig. 25. The case numbers refer to their order in Figs. 14 and 15.

It is seen that for all cases, both the improved model and series expansion provide better agreement relative to the simple model. All but two cases (4 and 5, i.e. vertical and horizontal patterns, respectively), have a ratio below 4. For most of the cases the improved model shows a better agreement than the Fourier series, except for cases 1, 4 and 5 (all drums, even pattern and vertical pattern, respectively).

Considering the simple model, the all drums case has the worst agreement to the model. This result should not be surprising, since the simple model is, generally speaking, less valid for large perturbations, and this is the largest perturbation examined.

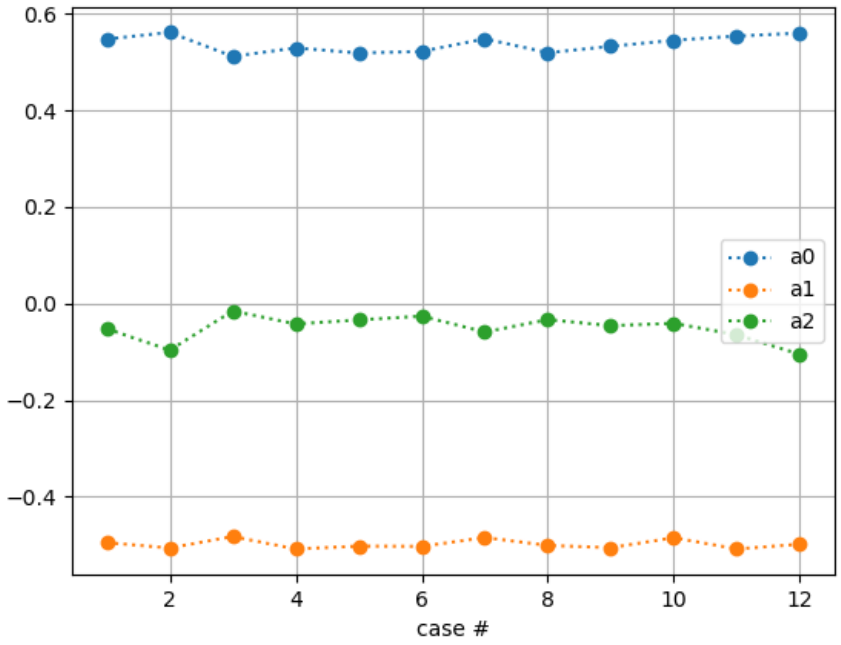

Figure 23. Coefficients of the Fourier series fit for all 12 cases.

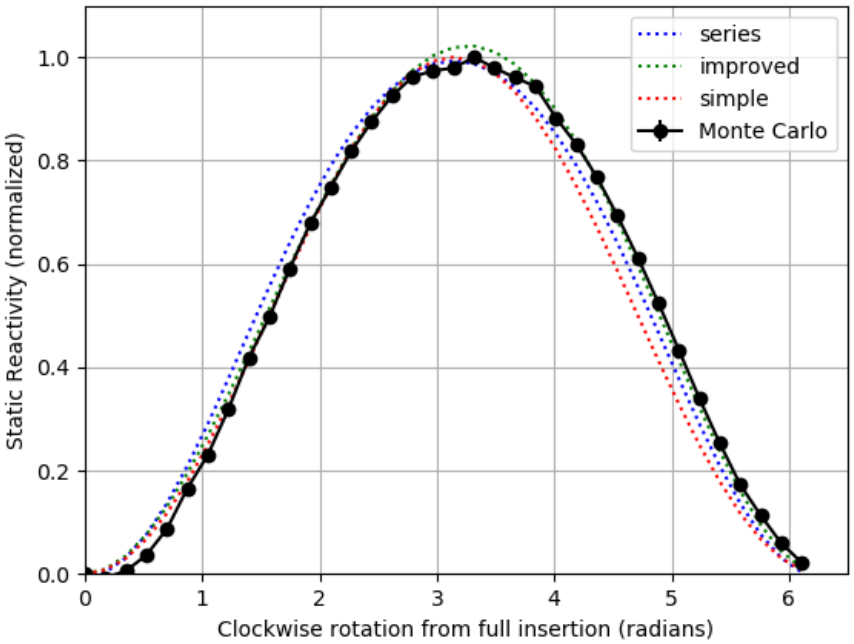

Figure 24. Integral worth curve for the case of horizontal pattern. Monte Carlo data is depicted against three analytical curves: physical models (simple and improved), and a Fourier series.

We note that cases 5, 6 and 8 (vertical, horizontal and diagonal odd patterns, respectively) show the worst agreement for both the improved model and the series expansion. By inspecting Fig. 14, these cases posses the strongest asymmetry, and the Fourier series expansion would likely still produce symmetric functions. That the improved physical model does not agree well suggests that the assumptions in this model (e.g. the $1/r^2$ dependence) lose their validity.

Finally, compared to the simple model, we attribute the better agreement of both improved and the series models to the higher frequency terms that can capture some perturbations to the fundamental cosine shape. In the case of the series expansion, these terms are readily obtained in the expression ((e.g. $\cos(2\theta)$), while in the improved model they can be derived by expanding the parabolic correction factor in harmonic series.

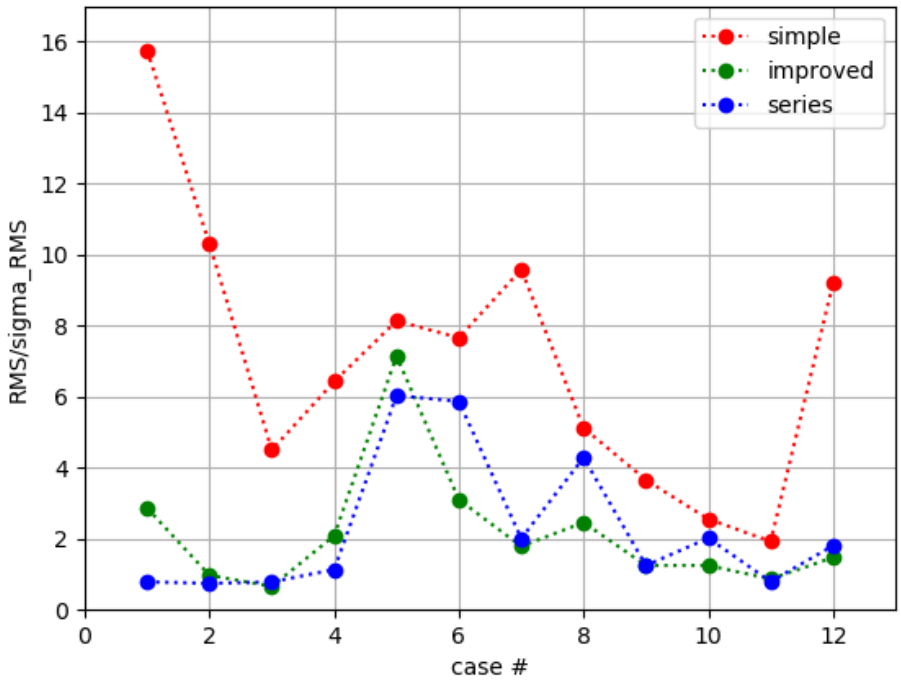

Figure 25. Comparison of RMS/σ_{RMS} between three analytical methods: physical model (simple and improved) and Fourier series expansion.

5. EVALUATION OF LOCAL TEMPERATURE AND REFLECTOR CONTROL SYSTEM CONCEPTS

5.1 Summary of Required Temperature or Reflector Reactivity

From Section 2, the reactivity requirements for each of the FPO categories are combined into Table 15. These are the essential *minimum* reactivity requirements that would be needed for a control system just for FPO–as opposed to FPO and shutdown.

Table 14. Summary of Reactivity Requirements for Load Follow by Category

Category	Ramp Rate ($\%P_r$/min)	Power Range Low / High ($\%P_r$)	Required $\|\rho\|$ (pcm)	Note
1	3 - 5	50 - 100	758	EUR [1]
2	20	50 - 100	759	EUR, emergency [1]
3	5	50 - 100	758	USA, EPRI, INPO [2]
4	1	75 - 100	379	Belgium [2]
5	10	20 - 100	1213	Germany, design limit [2]
6	10 5 2	80 - 100 50 - 100 20 - 100	1214	Germany, operational limit [2]
7	10	0 - 100	1517	PBMR [**?**]

5.2 Flow rate requirements for reactivity control

In order to evaluate the feasibility of local reactivity control via passive flow controls, the amount of temperature change with mass flow rate ($\frac{\partial T}{\partial \dot{m}}$) was analyzed using SAM. A mass flow rate change of ±10% and ±20% and the corresponding average temperature change is calculated to be approximately -1.73 K/$\%\dot{m}$. The rate of reactivity change with mass flow rate can by calculated as

$$\frac{\partial \rho}{\partial \dot{m}} = \frac{\partial \rho}{\partial T}\frac{\partial T}{\partial \dot{m}} = \left(\frac{\partial \rho}{\partial T_m} + \frac{\partial \rho}{\partial T_f}\right)\frac{\partial T}{\partial \dot{m}} \tag{64}$$

?? shows the required ΔT and $\%\dot{m}$ corresponding to the reactivities in Table 15 based on Eq. (64).

Table 15. Summary of Flow Rate Requirements for Load Follow

Category	Required $\|\rho\|$ (pcm)	Required ΔT (K)	
Required $\%\dot{m}$ (%)			
1	758	115	66
2	759	115	66
3	758	115	66
4	379	58	33
5	1213	184	>100
6	1214	184	>100
7	1517	230	>100

From this initial estimate we clearly see that the amount of reactivity available through the passive flow controllers would insufficient or impractical for nearly all FPO scenarios. At a minimum it would require a 33% change in the entire core flow rate and 58K temperature rise everywhere in the core. While this change in flow rate may be possible, it likely would not perform well for the overall power conversion system and turbine dynamics. Therefore, the the passive variable flow controllers are not likely to be a viable option for meeting many FPO requirements.

However, such a system may still prove useful for local power shaping, additional protection in over-temperature transients, or much smaller power changes. Considering Eq. (46), essentially

15pcm of reactivity is needed for each % change in power. For example, using the data presented previously, it would be possible to obtain 5% variations in nominal power at BOL assuming a ~15% change in the flow rate of 8 fuel assemblies in each quadrant. This level of control appears to be much more feasible.

5.3 Control Drum System Control Requirements

Based on the data in Fig. 16 any of the 2-drum or 4-drum patterns would be suitable for FPO in the U.S. To meet the FPO requirements of categories 5 through 7, only the 4-drum (or greater) patterns would be sufficient. In Belgium, with the minimal requirements, 1- or 2- drum patterns would be sufficient. Thus, we conclude that the existing control drum design of the Holos reactor is capable of providing sufficient reactivity for flexible power operations.

6. CONCLUSIONS AND FUTURE WORK

6.1 Conclusions

In this report various categories of FPO were defined. For each category the requisite reactivity for meeting the FPO specifications was quantified using a point kinetics reactor model with 3-temperature feedback. The available reactivity in the reactor through temperature perturbations and the existing control drum systems were then quantified. Additionally, simple analytic models for characterizing the control drum worth as a function of rotation position were also developed for future use in the development and analysis of control algorithms for automated reactivity control.

Finally, the assessed reactivities were compared against the required reactivity. Here it was found that the existing control drum system would be sufficient for meeting reactivity requirements for any of the categorized FPO requirements. Conversely, the reactivity available through the varying flow rate was not sufficient for any of the FPO categories.

The concept of the passive flow controllers may still have value in other applications such as local power shaping, additional margin and protection in over-temperature transients, and small power changes (e.g. < 10% rated power).

6.2 Future Work

Future work on this project will shift the technical focus and pursue the development and analysis of control algorithms for the reactor based on the control drums. As warranted, additional activities could also include

- further refinement of analytical models for the control drum worth curves
- feasibility investigation of passive variable flow controllers for non-FPO operation
- refinement of the reactor state-space model

REFERENCES

[1] A. Lohkov. "Technical and Economic Aspects of Load Following with Nuclear Power Plants." Technical report, NEA/OECD, Vienna, Austria (2011).

[2] "Non-baseload Operation in Nuclear Power Plants: Load Following and Frequency Control Modes of Flexible Operation." Technical report, International Atomic Energy Agency, Vienna, Austria (2018). URL http://www.iaea.org/Publications/index.html.

[3] V. Seker and B. Kochunas. "Assessment of Local Temperature Reactivity Response in Multi-Module HTGR Special Purpose Reactor." Technical Report NURAM-2020-002-00, University of Michigan, Ann Arbor (2020).

[4] B. Kochunas, K. Barr, and S. Kinast. "Assessment of Variable Reflector Reactivity Envelope in Multi-Module HTGR Special Purpose Reactor." Technical Report NURAM-2020-003-00, University of Michigan, Ann Arbor (2020).

[5] T. Stauff, N. and Lee, C. and Shriwise, P. and Miao, Y. and Hu, R. and Vegendla, P. and Fei. "Neutronic Design and Analysis of the Holos-Quad Concept." Technical report, Argone National Laboratory (2019).

[6] "ARPA-E | Transportable Modular Reactor." URL https://arpa-e.energy.gov/?q=slick-sheet-project/transportable-modular-reactor.

[7] N. Stauff. "Design Specifications of the Holos-Quad." private communication (2020).

[8] S. Choi, S. Kinast, V. Seker, C. Filippone, and B. Kochunas. "Preliminary Study of Model Predictive Control for Load Follow Operation of Holos Reactor." *Transactions of the American Nuclear Society*, **volume 122**, pp. 660–663 (2020). URL https://dx.doi.org/10.13182/T122-32327.

[9] C. E. García, D. M. Prett, and M. Morari. "Model predictive control: Theory and practice—A survey." *Automatica*, **volume 25**(3), pp. 335 – 348 (1989). URL http://www.sciencedirect.com/science/article/pii/0005109889900022.

[10] L. Wang. *Model predictive control system design and implementation using MATLAB®*. Springer Science & Business Media, London, UK (2009).

[11] J. Leppänen, M. Pusa, T. Viitanen, V. Valtavirta, and T. Kaltiaisenaho. "The Serpent Monte Carlo code: Status, development and applications in 2013." *Annals of Nuclear Energy*, **volume 82**, pp. 142–150 (2015).

[12] R. Hu. "SAM Theory Manual." Technical report, Argonne National Laboratory (2017).

[13] J. Lee. *Nuclear Reactor Physics and Engineering*. John Wiley & Sons, Inc, Hoboken, NJ, USA (2019).